Plasma Sources
Science and
Technology

ACCEPTED MANUSCRIPT

Investigation of the diffusive ionization wave in double-pulse experiment in low-pressure air-like mixtures

To cite this article before publication: Yulin Guo *et al* 2025 *Plasma Sources Sci. Technol.* in press https://doi.org/10.1088/1361-6595/adf575

Manuscript version: Accepted Manuscript

Accepted Manuscript is “the version of the article accepted for publication including all changes made as a result of the peer review process, and which may also include the addition to the article by IOP Publishing of a header, an article ID, a cover sheet and/or an ‘Accepted Manuscript’ watermark, but excluding any other editing, typesetting or other changes made by IOP Publishing and/or its licensors”

This Accepted Manuscript is **© 2025 IOP Publishing Ltd. All rights, including for text and data mining, AI training, and similar technologies, are reserved.**.

During the embargo period (the 12 month period from the publication of the Version of Record of this article), the Accepted Manuscript is fully protected by copyright and cannot be reused or reposted elsewhere.

As the Version of Record of this article is going to be / has been published on a subscription basis, this Accepted Manuscript will be available for reuse under a CC BY-NC-ND 4.0 licence after the 12 month embargo period.

After the embargo period, everyone is permitted to use copy and redistribute this article for non-commercial purposes only, provided that they adhere to all the terms of the licence https://creativecommons.org/licences/by-nc-nd/4.0

Although reasonable endeavours have been taken to obtain all necessary permissions from third parties to include their copyrighted content within this article, their full citation and copyright line may not be present in this Accepted Manuscript version. Before using any content from this article, please refer to the Version of Record on IOPscience once published for full citation and copyright details, as permissions may be required. All third party content is fully copyright protected, unless specifically stated otherwise in the figure caption in the Version of Record.

View the article online for updates and enhancements.

This content was downloaded from IP address 1.80.1.88 on 03/08/2025 at 19:57

Investigation of the diffusive ionization wave in double-pulse experiment in low-pressure air-like mixtures

Yulin Guo[1], Yaqi Zhang[1], Yifei Zhu[1], Anbang Sun[1,*] and Pierre Tardiveau[2,*]

[1]School of Electrical Engineering, Xi'an Jiaotong University, State Key Laboratory of Electrical Insulation and Power Equipment, Xi'an, 710049, China
[2]Laboratoire de Physique des Gaz et des Plasmas, CNRS, Universite Paris-Saclay, Orsay 91400, France

E-mail: anbang.sun@xjtu.edu.cn and pierre.tardiveau@universite-paris-saclay.fr

Abstract

In this work, we experimentally and numerically investigated positive and negative diffusive ionization wave characteristics under a double voltage pulse scheme in low-pressure (200 mbar) Nitrogen/Oxygen mixtures. In the experiment, we recorded the characteristics of both first and second discharges. In the simulation, we fully simulated two consecutive discharges and obtained similar results to the experiment with the positive discharge. For the first discharge, positive ionization wave width and length decrease with oxygen concentration, while negative discharge remains consistent but with a worse repeatability. During the second pulse, positive discharge shrinks in morphology but maintains propagation velocity due to the quasi-neutral plasma shielding effect s at the second discharge, which is reproduced and explained through a 2D fluid model. The second negative discharge exhibits pulse-interval-dependent branching probability (increasing then decreasing with pulse interval), which is observed across all tested mixtures. Combined simulation-experiment analysis excluded the effects of residual charge and gas temperature in this branching process: On the one hand, the residual charge density becomes very low and uniformly distributed after the long pulse interval. On the other hand, even under double pulses with the lowest intervals, the gas temperature increase remains limited. Finally, through modeling on the shock wave generated by the first discharge, we attributed negative discharge branching to shockwave-induced gas density gradients near the electrode. The higher gradient surface and lower head electric field of the negative discharge compared to the positive causes localized protrusions, which then grow into filament streamers.

1 Introduction

Nanosecond pulsed diffusive discharges generated by extreme overvoltage with a short rising edge can provide high electron energy and plasma reactivity and thus is promising for applications in the future [1-3]. In order to better meet the plasma characteristics in required applications, repetitively pulsed discharges are often used to generate highly reactive species[4, 5]. However, due to the introduction of multiple voltage pulses, the characteristics of a discharge will be greatly influenced by previous ones, which can even lead to discharge mode transition (streamer to filament, streamer to spark)[6, 7]. The mechanism involved is universally described as a 'memory effect'[8, 9]. In previous works, the memory effect is often summarized as the results of residual charges[10], metastable species[11, 12], or gas temperature increase[13]: i) metastable species are usually considered as the dominant effect because of their relatively long lifetime during the pulse interval. ii) the reduced field strength increases with gas temperature and a shock wave created[14, 15] due to the fast gas heating processes. iii) residual charges, especially free electrons, can guide subsequent positive streamers but have a negligible effect on negative streamers [8].

However, when multiple discharges accumulate and cause changes in plasma characteristics, often two or more of the aforementioned mechanisms exist simultaneously[9], making difficult to investigate any single mechanism. Therefore, many researchers use special experimental or numerical methods to 'decouple' these mechanisms: Naidis *et al* [16] used a 1D simplified energy deposition equation and considered the influence of thermal effect to investigate the spark formation process. Tholin and Bourdon [17, 18] simulated how the ionization level and gas temperature influence discharge channel formation through separate settings of pre-ionization and heating level in the model. Yuan *et al* [19] and Zhao *et al* [20] simulated the residual charge of previous discharges by pre-placing a plasma patch in the positive and negative streamer channel.

Among all the methods, the 'double-pulse experiment' is a special experimental method that only focuses on two consecutive pulses instead of multiple discharges. This method enables one to investigate in detail the influence of the first discharge on the characteristics of the second one, such as discharge morphology, propagation velocity, etc. Nijdam *et al* [21] investigated the relation between two consecutive streamers in different gas mixtures through double-pulse experiments, and found that the propagation behavior of the second positive streamer varies significantly with the pulse interval. Short pulse intervals (nanoseconds) cause the second streamer to follow the first streamer's path. Intermediate intervals (microseconds) lead to propagation along the previous channel edges, bypassing the 'inception cloud', the approximately spherical main body of the initial streamer. Longer intervals (milliseconds) allow subsequent streamers to overlap previous channels or develop independently. Later, Li *et al* [22] discussed the streamer inception characteristics through double-pulse experiments, and they concluded that the subsequent streamers are generally longer than their predecessors because of a faster inception. Kazemi *et al* [23] studied the relationship between the current amplitude of the subsequent positive corona and the double-pulse interval, and found that when the double-pulse interval time is short (hundreds of microseconds), the current amplitude of the subsequent corona discharge is significantly lower than that of the first one. As the pulse interval increases, the current amplitude of the subsequent corona discharge gradually increases and approaches that of the first corona discharge (microsecond). With a similar method, Zhang *et al* [24] studied the influence of a previous corona discharge on the subsequent streamer morphologies. They found that subsequent streamers tend to be weaker and shorter at a long pulse interval while longer and brighter when no pulse interval is set.

In simulations, 0D model is often used to calculate the time-dependent species evolution in repetitive discharges to consider as many reactions as possible while saving computing resources. For example, Nijdam *et al* [21] explained the double-pulse experiment results on streamer continuation through the electron density estimation with a 0D model. However, for streamer behaviors under longer pulse intervals, 0D model is difficult to give a good explanation on the streamer morphology differences, in this case, a higher dimensional model is needed. By combining 2D and 0D models, both short-duration nanosecond discharge development (2D) and long-duration post-discharge (0D) can be calculated. For example, Chen *et al* [25] used the results of a 2D model as an input for a 0D model to propose a temperature criterion of streamer-to-spark transition. In an ideal situation, it will be more accurate to calculate two consecutive discharges (including a pulse interval) directly through a 2D or 3D model. For example, Malla *et al* [26] used a 2D fluid model based on the *Afivo-streamer* framework to calculate two consecutive streamers to reproduce the streamer continuation and re-inception phenomena in Nijdam's work [21] considering 56 species and 263 reactions. However, this is very uncommon in other models: it will take a lot more calculation time and resources, and in these models, reactions, gas heating processes and shockwave that may occur during the pulse interval usually cannot be fully discussed.

The diffusive discharge characteristics under repetitive pulses haven't been systematically investigated before. On the one hand, to further promote its practical application, the repetitive diffusive discharge must be studied. On the other hand, unlike filamentary streamers, its diffusive discharge morphology and high discharge repeatability make it a natural research object to study the discharge characteristics under uniform background ionization. In this work, we investigated both positive and negative diffusive ionization wave characteristics in different N_2/O_2 mixtures through a double-pulse experiment and tried to fully model two consecutive discharges through a 2D fluid model. The experiment setup and model description are introduced in section 2. The experiment results under the double-pulse scheme are shown in section 3, and the discussion and modeling results are shown in section 4.

2 Experimental setup and numerical model

In this work, we investigated the diffusive ionization wave characteristics through experiments that found completely different phenomena between positive and negative discharges and tried to use a 2D fluid model to explain the differences.

2.1 Experimental platform

The experimental platform used to investigate the diffusive ionization wave is shown in Fig. 1. A nanosecond pulse generator (FID FPG 50-50NX2) is used as a voltage source, and it is connected to a tungsten needle electrode. The tip radius *r* of the needle electrode is 100 μm (the measurement error is within 5 μm), the radius of the plate electrode is 10 cm, and the electrode space *d* is 16 mm. The discharge voltage and current are measured through a high-voltage probe (Tektronix P6015A) and a Rogowski coil respectively. High voltage and current waveforms are recorded through an oscilloscope (Tektronix MDO34 1GHz). Short exposure discharge images are captured by an ICCD camera (Andor iStar DH334T). Oxygen concentration and pressure of the gas mixtures are controlled through the gas flow meters. In this work, oxygen concentrations are mainly kept at 20%, 1%, and pure nitrogen(99.9999%) to investigate the influence of oxygen concentration. Meanwhile, the gas pressure is kept at 200 mbar in this work and the chamber is pumped to less than 5×10^{-5} Pa before each experiment to ensure the purity of the gases. By taking into account the error of the flow meter and discharge chamber airtightness reasons, the 'pure nitrogen' experiment will inevitably contain ~10ppm oxygen.

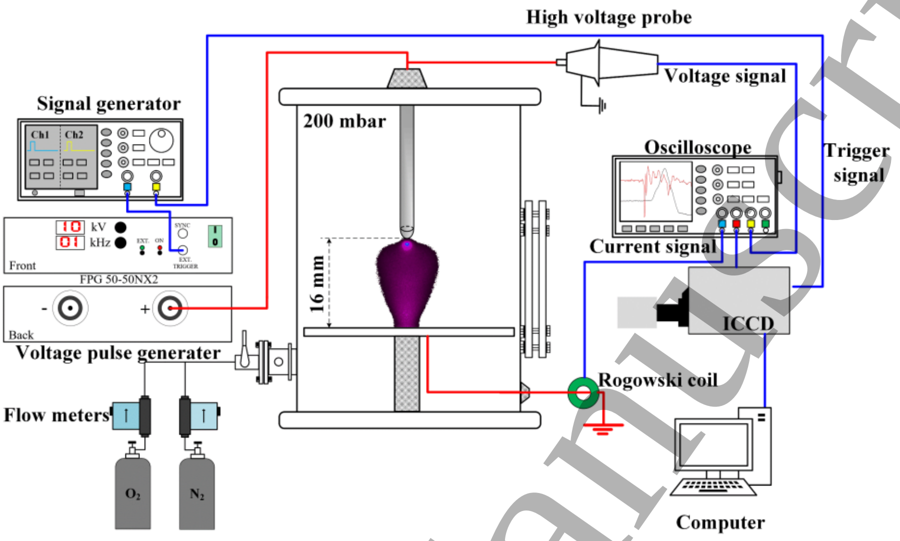

Fig. 1 Experimental setup. Red lines represent the measurement signal and blue lines represent the control signal.

2.2 Double pulse setup

Typically applied voltage profiles in our experiments are shown in Fig. 2. The positive polarity reaches its maximum value of 17.4 kV at 14.8 ns, and the negative polarity reaches its minimum value of -18.4 kV at 15 ns. The rising time (from 0 kV to its peak value) for both polarities is about 15 ns, and the pulse width is about 25 ns.

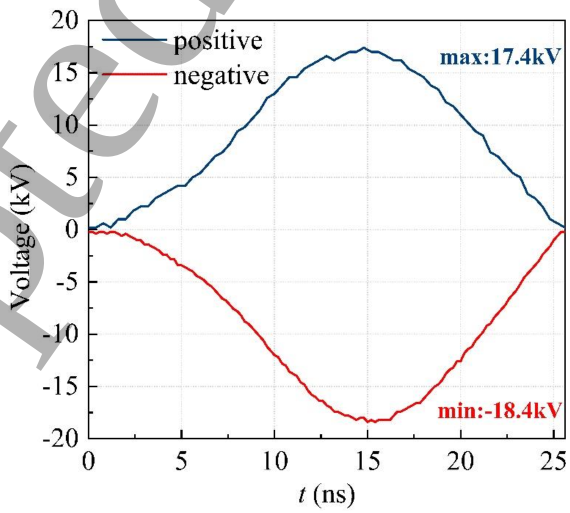

Fig. 2 The typical applied single pulsed voltage profiles for both positive and negative polarity.

To investigate the discharge characteristics under the memory effect, the double-pulse set-up is introduced in this work. The discharge triggering signals are set as shown in Fig. 3. In each period, two trigger pulses are applied and both signals will trigger the nanosecond pulse generator and then generate a voltage pulse (can either be a positive or negative pulse shown in Fig. 3). In the experiment, the pulse interval Δt between the two trigger pulses is set to 20μs, 200μs, 1ms, 10ms, and 100ms to investigate the second discharge characteristics when a first discharge exists. Also, when taking photos and optical emission spectroscopy signals, repeated experiments are needed, and to minimize the influence between two experiments, the overall trigger interval of the double pulses is set to 20 seconds, ensuring the independence of each double-pulse in repeated experiments.

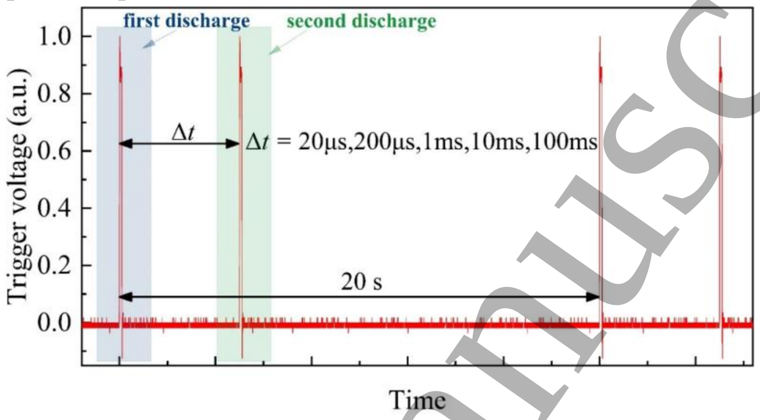

Fig. 3 The double-pulse scheme triggering signal.

2.3 Numerical method

The numerical model we use is the 2D fluid model *PASSKEy* (PArallel Streamer Solver with KinEtics)[27] using the local mean energy approximation, which is proved to be more accurate at lower pressure cases with smaller mesh refinement[28, 29]. When it comes to the diffusive ionization wave, this model has been proven valid in previous works [29, 30], in which we achieved good agreements with both 200 mbar and 1000 mbar diffusive ionization wave experiments in both macroscopic discharge characteristics [31] and electric field measurements[32]. In this work, we use a 4 cm×4 cm domain shown in Fig. 4 to simulate the discharge. The pin electrode shape, applied voltage, and gas mixtures are set exactly the same as the experiment profiles. The governing equations of the 2D model are shown in equation (1)-(3): Poisson's equation solving the electric field is shown in equation (1), the drift-diffusion equations for species are solved in equation (2), and the generalized Helmholtz equations solving photoionization function is shown in equation (3). Within the computational framework, the Euler equations are solved to determine the gas temperature. For a detailed account of the coupling methods, refer to [25].

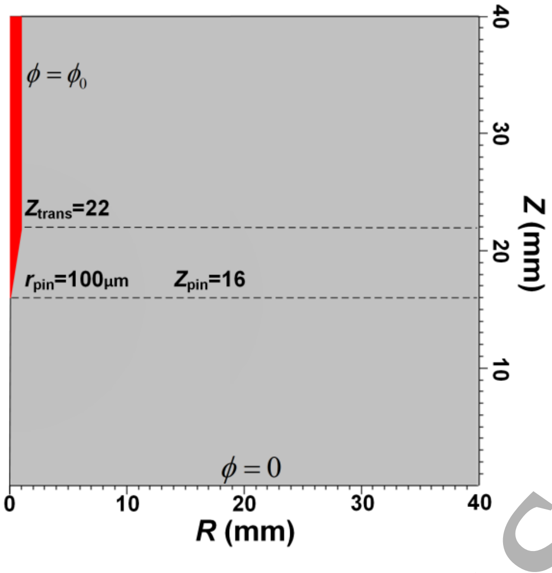

Fig. 4 The computational domain in the simulation.

$$\nabla(\varepsilon_0 \varepsilon_r \nabla \varphi) = -\sum_{i=1}^{N} q_i n_i \qquad (1)$$

$$\frac{\partial n_i}{\partial t} + \nabla \cdot \mathbf{\Gamma}_i = S_i + S_{\text{ph}} \qquad (2)$$

$$S_{\text{ph}} = \sum_j S_{\text{ph}}^j \qquad (3a)$$

$$\nabla^2 S_{\text{ph}}^j(\vec{r}) - (\lambda_j p)^2 S_{\text{ph}}^j(\vec{r}) = -A_j p^2 \frac{p_q}{p + p_q} I(\vec{r}) \qquad (3b)$$

$$\frac{\Psi_0(r)}{p} = (pr) \sum_j A_j \mathrm{e}^{-\lambda_j pr} \qquad (3c)$$

$$\frac{\Psi_0(r)}{p} = \frac{1}{4\pi} \frac{\omega}{\alpha_{\text{eff}}} \frac{\int_{\lambda_{\min}}^{\lambda_{\max}} \xi_\lambda (\mu_\lambda / p) \exp((-\mu_\lambda / p) pr) I_\lambda^0 d\lambda}{\int_{\lambda_{\min}}^{\lambda_{\max}} I_\lambda^0 d\lambda} \qquad (3d)$$

In equation (1), φ is the electric potential, q_i is the charge for species, and ε are the permittivities of vacuum space and the relative permittivity. For Poisson's equation, Neumann conditions are used far from the plasma generation region in the gap, and Dirichlet conditions are used on the pin and plane electrodes. In equation (2), n_i and S_i are the density and source term of species, and S_{ph} is the photon ionization source term. For the negative discharge, ion-induced secondary electron emission on the cathode surface is very important, and the emission coefficient γ is set to 0.01. In equation (3), λ_j and A_j are fitting coefficients for photoionization functions, p is the gas pressure, p_{q} is the quenching pressure, $\Psi_0(\text{r})/p$ is the photoionization function, ω is the excitation coefficient, α_{eff} is the effective Townsend ionization coefficient, μ_λ and ξ_λ are the absorption coefficient and spectrally resolved photoionization yield, λ is the spectral range of the radiation, and I_λ^0 is the spectral density of ionizing radiation. The description of the generalized Helmholtz equations is thoroughly explained in [29, 30].

In this work, we try to fully simulate two consecutive discharges, thus a reaction system that considers more comprehensive electron-ion and ion-ion recombination, negative/positive ion conservation reactions is built, referring to the work of Guo *et al* [33] on the choice of a reaction system in air. The reactions used in the present work are shown in Table A1 in Appendix. A. The initial conditions for the charged species used in the simulation are uniformly distributed 8×10^7 m^{-3} N_2^+, 2×10^7 m^{-3} O_2^+, and 10^8 m^{-3} electron.

3. Experiment results

3.1 Positive ionization wave

First, experiments on the positive diffusive ionization wave under single pulse (also can be recognized as the first discharge in the double-pulse scheme given the fact that we used a 20 s repetition rate) are conducted.

The development of the positive diffusive ionization wave in the 20% oxygen gas mixture is shown in Fig. 5. It's worth noting that the ionization wave ignites at *t*=4.4 ns(3.8 kV) in Fig. 4, and recorded this inception time as 0 ns in Fig. 5. It shows that the positive ionization wave propagates first as a spherical shape(0 ns - 3 ns) then as a conical shape(4 ns - 5 ns), and reaches the plane electrode at 5 ns after its inception. The discharge reaches its maximum width when reaches the plane electrode.

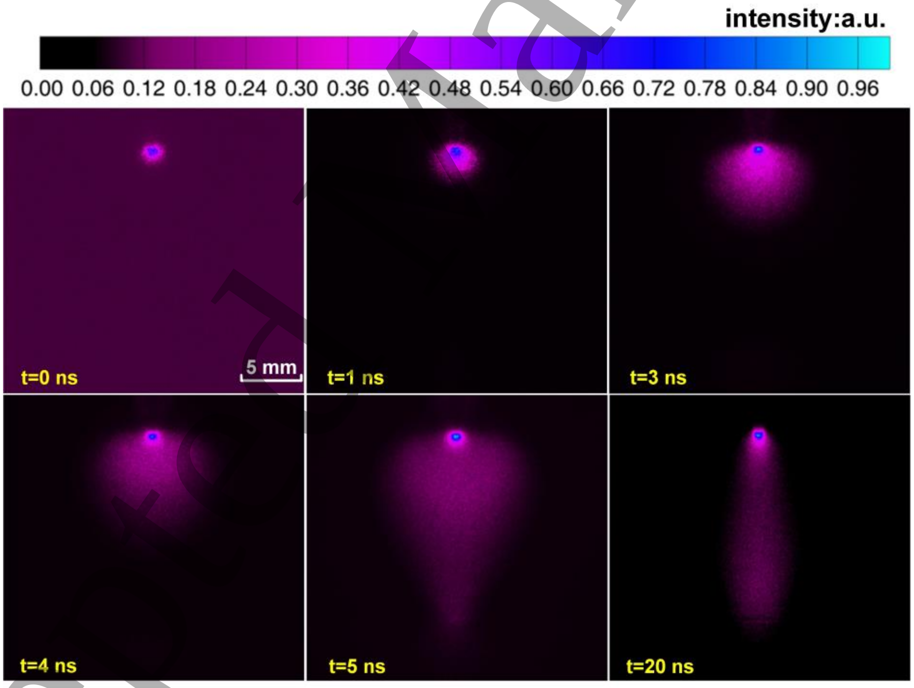

Fig. 5 The positive ionization wave development in 20% oxygen gas mixture. The camera gate is set to 2 ns, and each image is accumulated by 20 discharges.

Positive diffusive ionization wave characteristics in different oxygen concentrations are also recorded. Similar to our previous work [30], the discharge does NOT branch in pure nitrogen (contains ~10 ppm oxygen).

The discharge characteristics (to obtain the local emission, rather than emission integrated along the focus line, we conduct Abel inversion using the method described in [34]) in 20%

mixture, 1% mixture, and pure nitrogen are shown in Fig. 6. Note that to keep the consistency of research, we adopted the same method of calculating the discharge boundary in [30] and used the same criterion. The reason for the non-zero length and width at t=0 ns is that this time point is defined as the moment when initial light emission is first detected by the ICCD camera. By the time emission becomes detectable, the ionization wave has already developed to a certain size. With the decrease of oxygen concentration in the gas mixtures, the ionization wave width shrinks, and the ionization wave reaches the plane electrode later. Given that the dominant photoionization mechanism in N_2/O_2 mixtures is the ionization of ground-state O_2 by photons emitted during the de-excitation of singlet states N_2. Therefore, a decrease in oxygen content results in fewer O_2 molecules being ionized through this process, thereby reducing the additional electron source to the ionization wave. This further leads to a decrease in both the propagation velocity and width of the ionization wave.[35]. A separate discussion is required for the 'pure nitrogen' case, as positive ionization wave propagation necessitates background or photoionization sources. The experimental setup, with an overall repetition frequency of 0.05 Hz (20 s period) at 200 mbar, provides a baseline level of background ionization. Regarding photoionization, while the primary mechanism involving O_2 is absent, as reviewed in [36], photons emitted during the de-excitation of excited nitrogen atomic ions (produced from N_2 dissociation by energetic electrons) contribute minimally. The intensity of this photoionization source is substantially lower than that available in the 20% and 1% O_2 mixtures. Thus, in 'pure nitrogen', positive ionization waves maintain a diffuse morphology, albeit with slower propagation and a narrower structure.

The maximum ionization wave width is 12.5 mm in both 20% and 1% mixture and is 11.6 mm in pure nitrogen. In both 20% and 1% mixtures, the maximum width appears at 5.5 ns, and at 6.0 ns in pure nitrogen, which is the exact moment the ionization wave approaches the plane electrode as mentioned before. After that, the width of the ionization wave gradually decreases. Fig. 6(b) shows the ionization wave reaches the plane electrode at 5 ns in 20% mixture, 5.5 ns in 1% mixture, and 6 ns in pure nitrogen. Besides, it is obvious that before 4.0 ns in the 20% and 1% mixture(4.5 ns in pure nitrogen), the ionization wave propagates with nearly the same velocity and a bit slower in 'pure nitrogen', but after that, its velocity greatly increases when approaching the plane electrode. At this time, the ionization wavefront propagates to Z=8 mm, reaching exactly halfway through the gap. The observed acceleration can be attributed to the approach of the ionization wavefront to the plane electrode and thereby the enhancement of the electric field, and the 8 mm (half of the gap distance), considering this work and previous experiments [34], serves as a critical reference point where this field enhancement whether becomes dominant.

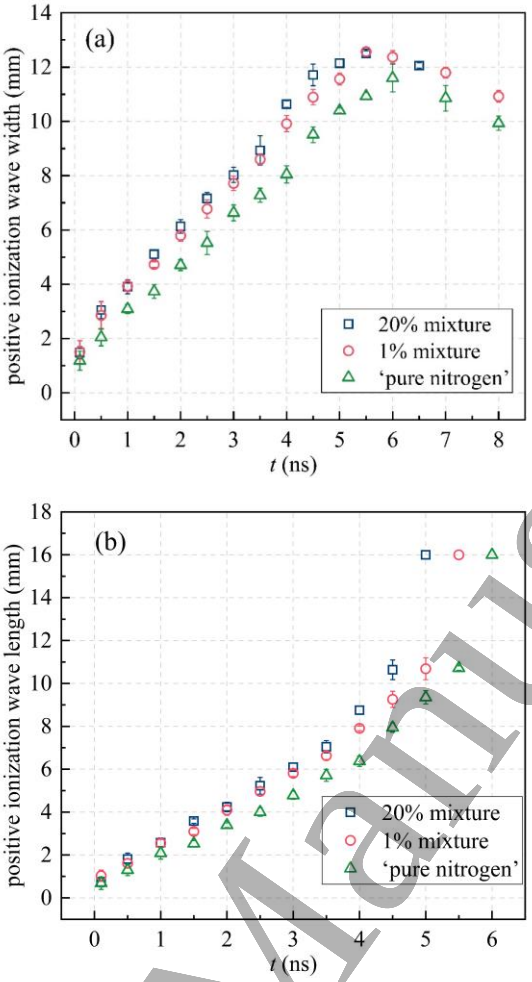

Fig. 6 The positive discharge characteristics in different oxygen concentrations. (a) is the discharge width and (b) is the length. Each point in the figure is the result of 50 measurements. Note that these values are taken after Abel inversion transform.

3.2 Positive ionization wave in double-pulse experiment

When the double-pulse scheme is applied, the second ionization wave keeps the same morphology but propagates with different characteristics.

Fig. 7 shows the ionization wave width after different pulse intervals Δ*t* (20 μs, 200 μs, 1 ms, and 10 ms) in different oxygen gas mixtures. In all three tested different gas mixtures, the maximum ionization wave width gradually increases with the pulse interval Δ*t*. Similar to Fig. 6(a), the ionization wave characteristics in 20% and 1% are similar.

Also, the difference between the first ionization wave width and the second one after Δ*t* =20 μs is smaller in pure nitrogen and the maximum width difference is 1.9 mm (see Fig. 7(c)), whereas the difference between these two discharges in the other two gas mixtures is very large (the maximum difference is ~3.8mm).

Besides, the results demonstrate two noteworthy characteristics:

- The first discharge width is nearly the same as the discharge width after Δ*t*=10 ms in all tested mixtures.
- In pure nitrogen, the discharge width after Δ*t*=20 μs, 200 μs, and 1 ms intervals are nearly the same.

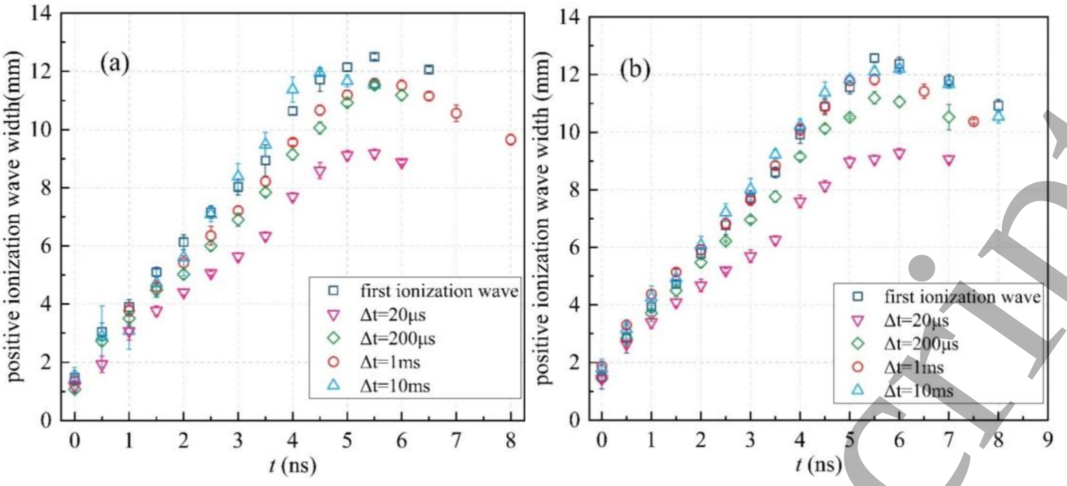

(a) Ionization wave width in 20% mixture. (b) Ionization wave width in 1% mixture.

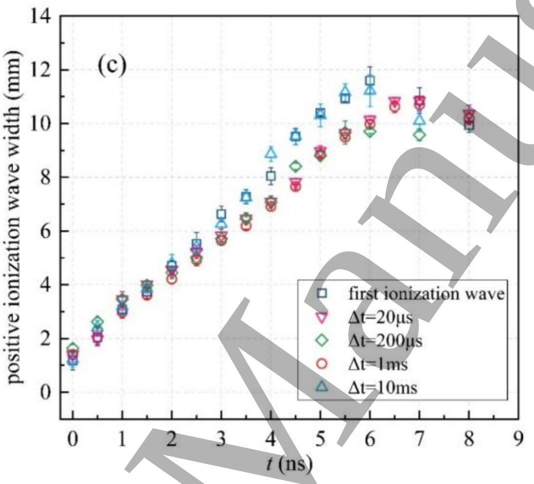

(c) Ionization wave width in pure nitrogen.

Fig. 7 The discharge width under the double-pulse scheme in different oxygen concentration mixtures. Each point in the figure is the result of 50 measurements.

Fig. 8 shows the diffusive ionization wave length after different pulse intervals Δ*t* (20 μs, 200 μs, 1 ms, and 10 ms) in different gas mixtures. No obvious differences can be observed except for their differences in ionization wave bridging time. In 20% mixture, the ionization wave bridges the two electrodes later at Δ*t*= 200 μs, 1 ms, but in pure nitrogen, it bridges earlier at Δ*t*= 200 μs, 10 ms but later at Δ*t*= 20 μs, 1 ms. This appears more as a stochastic rather than a discernible pattern. Nevertheless, it demonstrates that positive ionization waves maintain comparable propagation velocities during their development phases, regardless of variations in both pulse intervals and gas compositions.

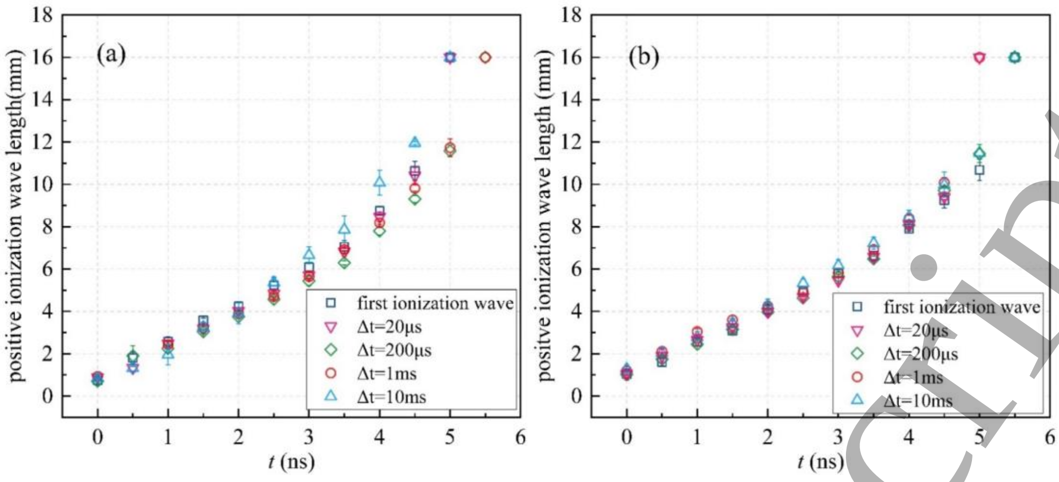

(a) Ionization wave length in 20% mixture. (b) Ionization wave length in 1% mixture.

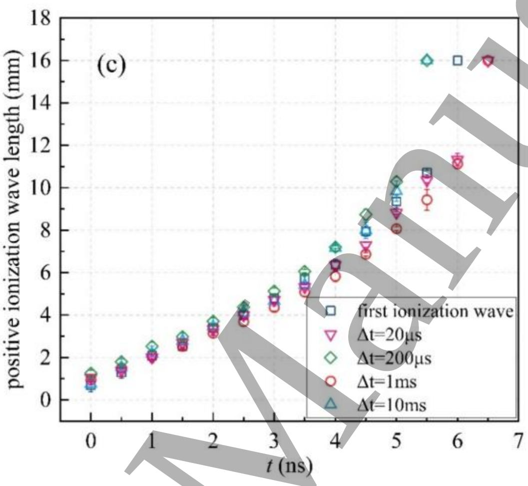

(c) Ionization wave length in pure nitrogen.

Fig. 8 The discharge length under the double-pulse scheme in different oxygen concentration mixtures. Each point in the figure is the result of 50 measurements.

The above results reveal that in all tested gas compositions, positive ionization waves become slimmer while maintaining comparable propagation velocities. Notably, the secondary discharge characteristics progressively resemble those of the first discharge with increasing pulse intervals, suggesting pulse interval-dependent recovery dynamics in the inter-pulse phase.

3.3 Negative ionization wave

First, experiments on the negative diffusive ionization wave under single pulse are conducted.

The development of the negative diffusive ionization wave in the 20% oxygen gas mixture is shown in Fig. 9. It incepts at *t*=5.8 ns(-6.2 kV) in Fig. 2, and time is recorded as 0 ns. Negative ionization wave also doesn't branch under this circumstance and propagates in a more diffusive way, and it also develops first with an almost spherical shape (0 ns - 2 ns) and then with a conical shape (3 ns - 5 ns). It reaches the plane electrode at 5.0 ns with maximum width. However, different from the positive ionization wave, there is a strong luminescence above the tip of the pin electrode, especially on both sides of the pin electrode. (see *t*=5 ns in both Fig. 5 and Fig. 9).

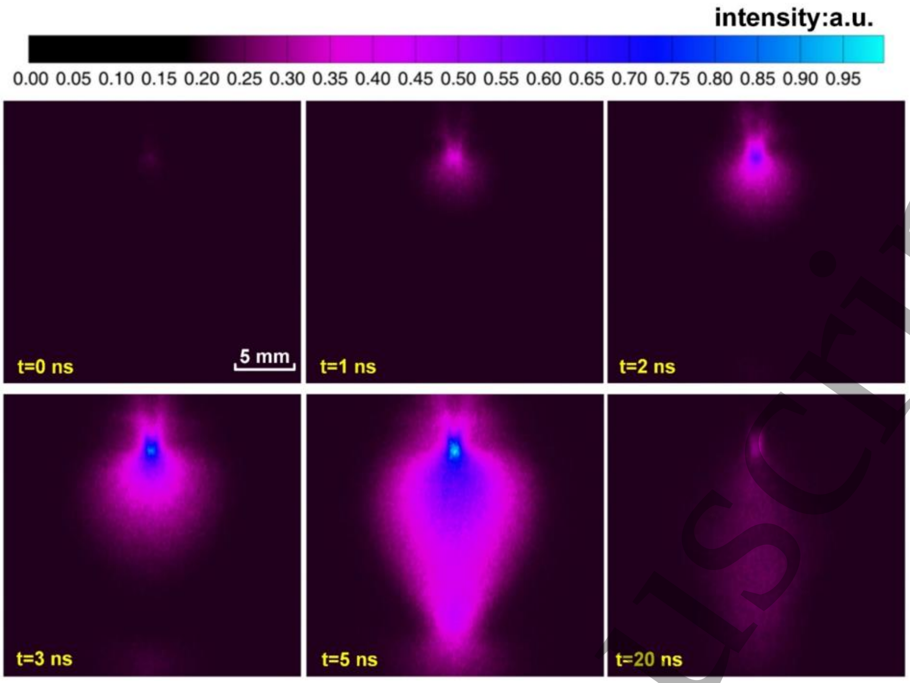

Fig. 9 The negative ionization wave development in 20% oxygen gas mixture. The camera gate is set to 2 ns, and each image is accumulated by 20 discharges.

Similar to the positive ones, the negative diffusive ionization wave keeps the same conical and diffusive shape in all the tested mixtures under single pulsed discharge, and its characteristics in 20% mixture, 1% mixture, and pure nitrogen are also recorded and shown in Fig. 10. Unlike positive ones, the width of negative ionization waves remains consistent across different gas mixtures. Alternatively, it could be argued that due to their bad repeatability, significant variations in the measured width are not apparent, with the discharge being only slightly wider in the 20% mixture. When it comes to the ionization wave length, the discharge in the 20% mixture is the first to reach the plane. In contrast, propagation in the 1% and pure nitrogen mixtures is somewhat slower.

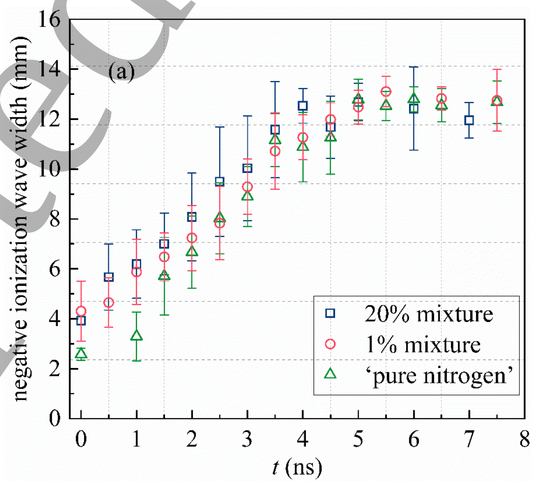

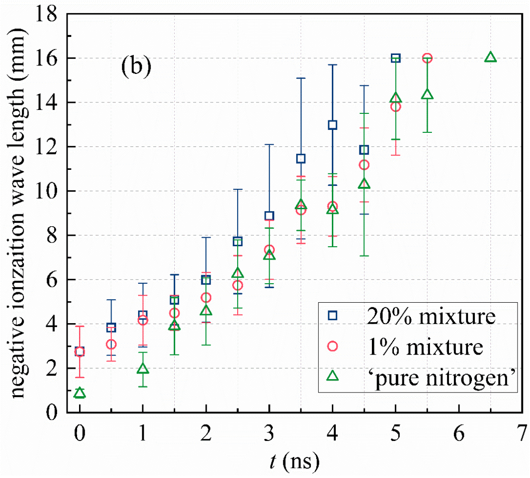

Fig. 10 The negative discharge characteristics in different oxygen concentrations. (a) is the discharge width and (b) is the length. Each point in the figure is the result of 50 measurements. Note that these values are taken after Abel inversion transform.

Overall, the negative ionization wave keeps a similar morphology in both width and length during the development in different gas mixtures. However, comparing the error bar in the single pulse positive and negative experiments, shows that there is a significantly higher stochasticity in negative discharges: even in 20% gas mixtures, instantaneous measurements show pronounced spatial variations, with maximum width deviations of ~4 mm(*t*=2.5 ns) and length discrepancies reaching ~6 mm(*t*=3 ns). Considering the electrode gap of 16 mm and maximum width of 12 mm, these fluctuations represent substantial statistical variations, which is conspicuously absent in positive discharges.

3.4 Negative ionization wave in double-pulse experiment

Different from the positive ionization waves, the negative ones have a certain probability of branching at the second discharge when the double-pulse scheme (with different pulse intervals Δt) is applied. The discharge morphology of the first and second discharge is significantly different as shown in Fig. 11. Note that when the negative ionization wave branches at the second discharge, it has different branch morphologies, and the figure only shows some of the examples. It can be observed that the branching morphologies are varied after Δt, a bright main streamer channel under the pin electrode often occurs (sometimes it splits into two streamers but most of the time there is a brighter channel). Besides, it's worth noting that in pure nitrogen at Δt=20 μs, the ionization wave remains diffusive but slightly slimmer than the first one.

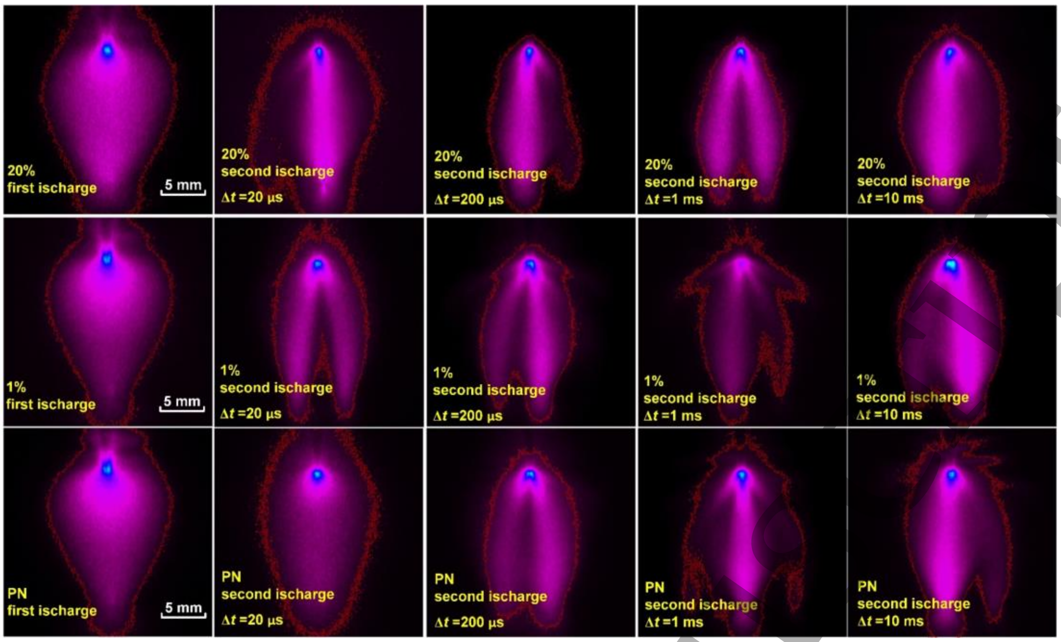

Fig. 11 The negative ionization wave morphology in different gas mixtures under the double-pulse scheme. The camera gate is set to 2 ns. The first column is the first discharge, and the rest is the second discharge after different pulse intervals Δ*t*.

To further explore the mechanisms of the negative ionization wave branching process at the second pulse, the branching probability (or frequency) under different Δ*t* is also investigated. Fig. 12 shows the experiment results on the branching probability, every situation is repeated 100 times and the number of times for branching is recorded (note that the time interval between each double-pulse train is 20 s, as shown in Fig. 3). In all the gas mixtures, the branching probability first increase then decrease with the pulse interval Δ*t* and the ionization wave rarely branches after 100 ms similar to the first pulse. The branching probability reaches its maximum at Δ*t*=200 μs in 20% and 1% mixtures and delays to Δ*t*=1 ms in pure nitrogen. As the oxygen concentration decreases, the maximum branching probability gradually increases: 78% in 20% mixture at 200 μs, 94% in 1% mixture at 200 μs, and 100% in pure nitrogen at 1ms.

In addition, there are still two points worth noting:

- Negative ionization waves also have a small chance of branching under the first pulse.
- The branching probability at Δ*t*=20 μs decreases with the oxygen concentration, and almost no branching is observed in pure nitrogen.

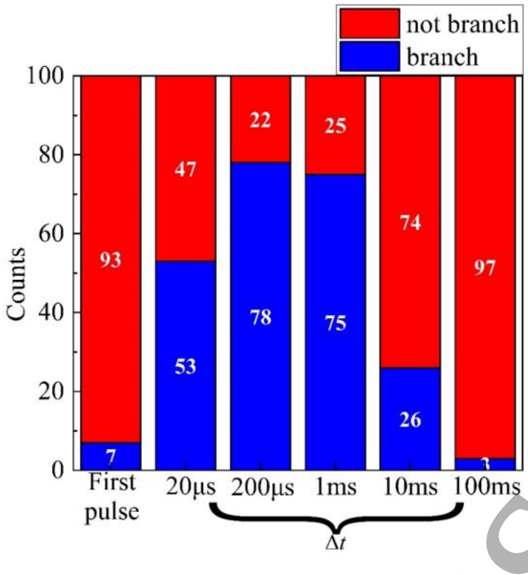

(a) The branching probability of the second discharge in 20% mixture.

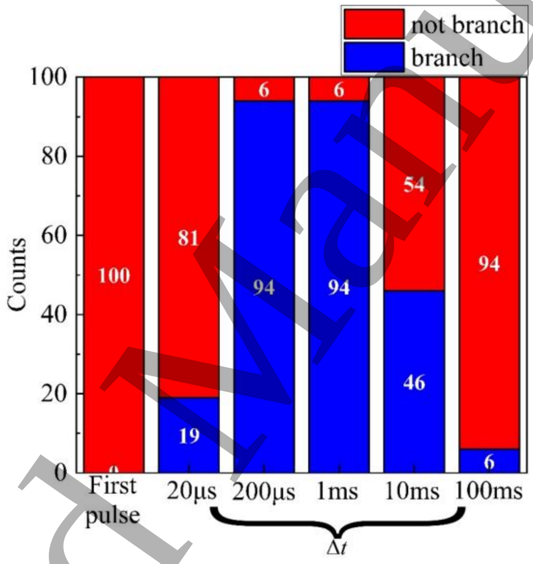

(b) The branching probability of the second discharge in 1% mixture.

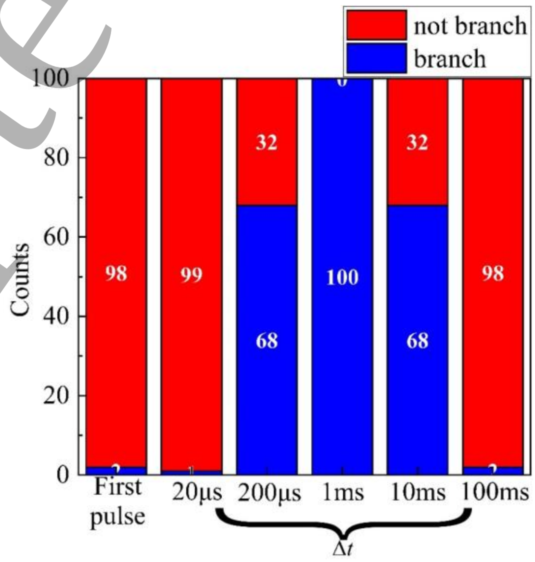

(c) The branching probability of the second discharge in pure nitrogen.

Fig. 12 The recorded branching probability of the negative discharge under the double-pulse scheme.

The first increase then decrease of the branching probability with Δ*t* indicates that a certain mechanism is playing an important role in this branching process under the influence of the first discharge. Since the propagation of the negative ionization wave leading to full gap breakdown and introduces additional complexities, the discharge gap is extended to 160 mm to simplify the system and specifically probe the branching mechanism. Within this longer gap, the discharge is limited to forming an 'inception cloud' near the pin druing the pulse duration. This allows for a focused investigation of whether branching occurs inherently within the negative discharge, isolated from full breakdown effects.

It is noted that in Fig. 12, the second discharge after a 100 ms Δ*t* restores its diffuse state in different gas mixtures. Therefore, measurements of the width and length of its ionization wave are performed and compared with the first discharge, with the results shown in Fig. 13 and 14. In terms of ionization wave width, the negative polarity discharge shows a slightly reduced average width compared to the first. As for length, the second discharge in various gas mixtures generally develops slightly faster than the first ionization wave, but within the same gas mixture, they reach the plane electrode at approximately the same time. Although the repeatability of the negative ionization wave is worse compared to the positive one, it still exhibits similar trends to the positive polarity (See the first discharge versus the second discharge after a 10 ms Δ*t* in Fig. 7 and Fig. 8).

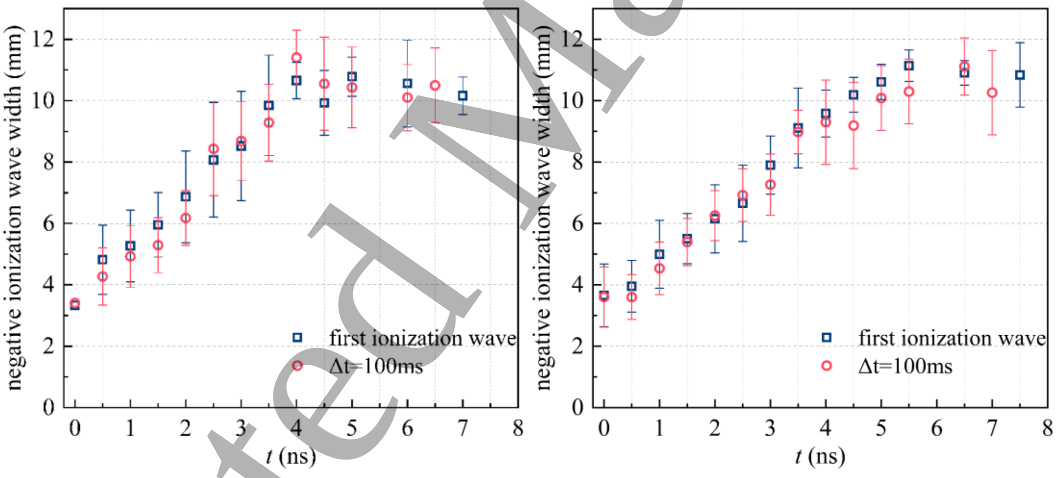

(a) Ionization wave width in 20% mixture. (b) Ionization wave width in 1% mixture.

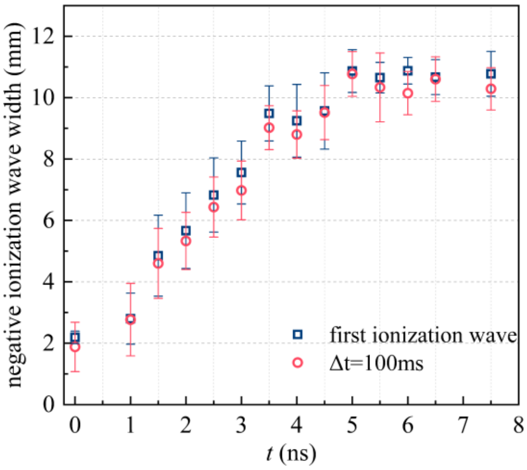

(c) Ionization wave width in pure nitrogen.

Fig. 13 The negative discharge width under the double-pulse scheme in different oxygen concentration mixtures. Each point in the figure is the result of 50 measurements.

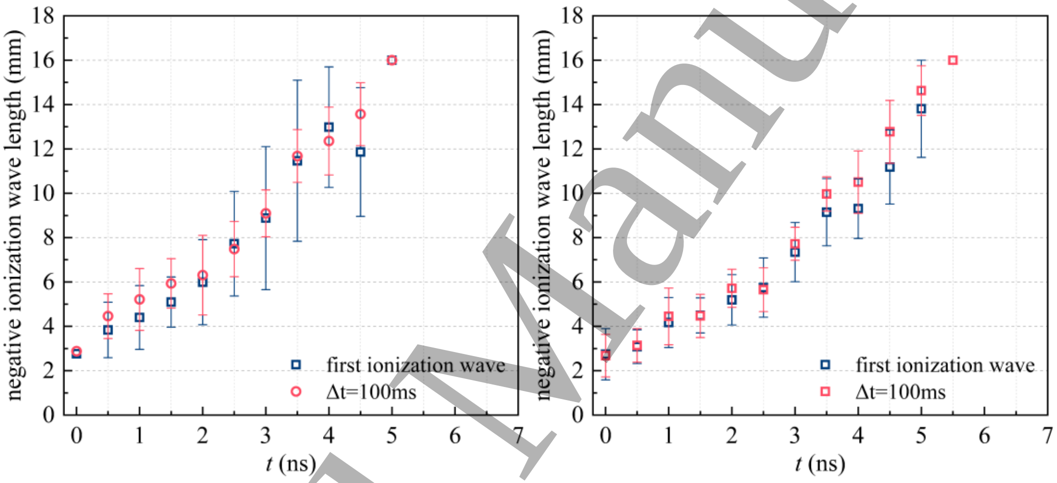

(a) Ionization wave length in 20% mixture. (b) Ionization wave length in 1% mixture.

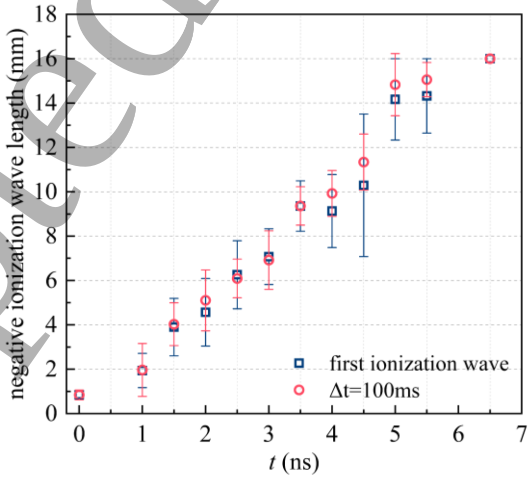

(c) Ionization wave length in pure nitrogen.

Fig. 14 The negative discharge length under the double-pulse scheme in different oxygen concentration mixtures. Each point in the figure is the result of 50 measurements.

3.5 The inception cloud under double-pulse experiment

The inception cloud is a stage between the avalanche and the elongated streamer in both positive and negative polarities[37, 38] and has been regarded as a similar phenomenon to the spherical ionization wave, which is the spherical propagation stage shown in the first row of Fig. 5 and 9.[39]. In Sections 3.2 and 3.4, we investigated the positive and negative ionization waves under double-pulse experiment. In this section, similar experimental phenomena (positive streamer doesn't branch and negative streamer branch under double-pulse scheme) should be observed on the inception cloud.

The gap distance is adjusted to 160 mm and other conditions (electrode shape, gas pressure, voltage profiles, etc) are kept, and the oxygen concentration is set at 20%. Under such a short-duration voltage pulse, the first inception cloud gradually expands but does not break up , a similar situation can also be found in the work in [40]. The discharge morphology under double-pulse is shown in Fig. 13. The inception cloud generated under positive pulse keeps the same morphology at different Δ*t*. The positive inception cloud characteristics are shown in Fig. 14, their difference in length and width is not large for various Δ*t*.

But for the negative inception cloud, it has a certain probability of branching after a pulse interval. Its branching probability is also recorded, and the results are shown in Fig. 15. The branching probability is similar to the negative ionization wave in 20% mixture (see Fig. 12(a)), and they both reach the maximum at Δ*t*=200 μs. Yet the branching probability of the inception cloud is higher than that of the negative ionization wave.

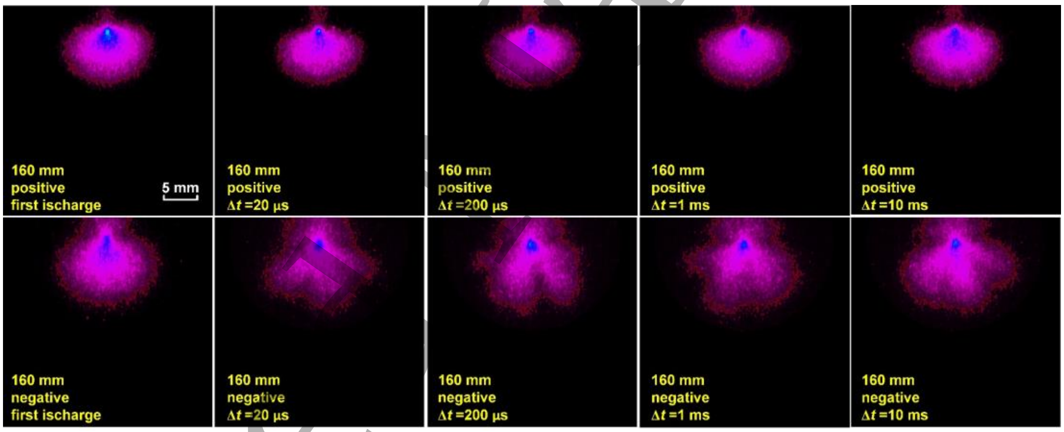

Fig. 13 The positive and negative inception cloud morphology in a 160 mm gap under double-pulse experiment. The oxygen concentration is set 20%, and the whole gap is not shown considering the luminous emission is localized near the pin electrode. The camera gate is set to 2 ns.

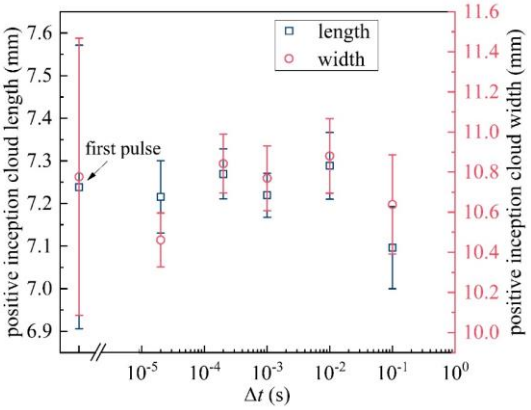

Fig. 14 The positive inception cloud width and length. The oxygen concentration is set 20%.

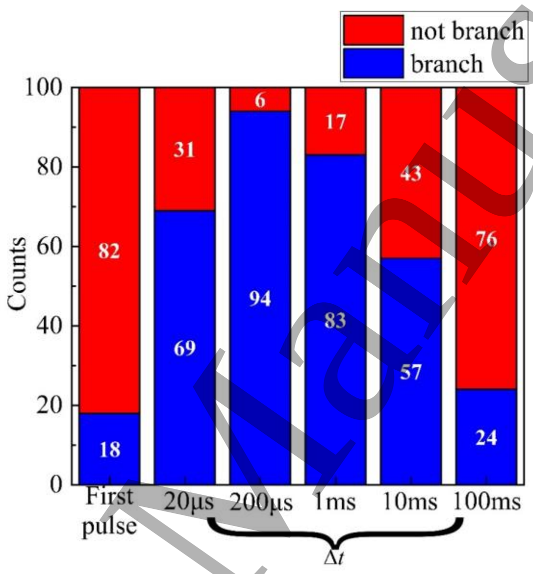

Fig. 15 The branching probability for the negative inception cloud. The oxygen concentration is set 20%.

The distinction in the morphology of the inception cloud and the branching probability between positive and negative polarities shows that the branching phenomenon in negative diffuse ionization waves is not unique but is a more general phenomenon under negative polarity voltage. Considering that the pulse width in this work is very short, the inception cloud cannot breaks up, let alone reach the plane electrode. Therefore, compared to diffuse ionization waves, it does not produce a very pronounced local temperature increase. Moreover, due to a smaller Laplacican field, its maximum electron density and ionization degree are also lower compared to diffuse ionization waves that can connect the two electrodes. Thus it can lead to a relatively faster dissipation of net charge in space over the same time. Due to the combined characteristics of low temperature indication and rapid charge dissipation, and the fact that it still produces branching under negative polarity, these experimental results suggest that the origin of branching in the second pulse under negative polarity may not be temperature or residual charges.

4. Discussion on the double-pulse experiment

By setting in the model the exact same input voltage profile, electrode geometry, and gas components as in the experiment, the discharge characteristics are calculated in this section to discuss the first and second discharge behaviors.

4.1 Characteristics of the first discharge:

As described in the last section, the discharge characteristics between positive and negative discharge during the first pulse are not so different except for the following ways:

- In the main discharge channel below the pin, the negative discharge has a larger high-light intensity area than the positive one(see below Fig. 16 row three, t=5 ns, light blue area).
- For negative discharges, strong linght emission is consistently observed at the pin electrode surface, whereas this is absent in positive ones.

To explain these differences, the simulated $N_2(C^3\Pi_u)$ density distribution is shown in Fig. 16. At 2 ns, the density is higher around the pin electrode in negative discharge, especially in the 16<Z<23 mm area. Secondary electron emission from the negative polarity electrode surface and the repulsion of those electrons from electrode cause this accumulation of electrons and further generate more light emission. At 5.5 ns after the discharge has bridged the two electrodes, the contour lines at 10^{17} m^{-3} show there is a larger light-emitting area near the pin electrode in the negative discharge. (The choose of this contour line is based on the work of Ren *et al* [41] on the simulation of negative diffuse discharges, where 10^{16}-10^{17} m^{-3} of ‘N_2C density’ serves as a discharge boundary.) The contour line at 10^{17} m^{-3} shows the negative discharge also has a larger width, making it look more ‘diffusive’.

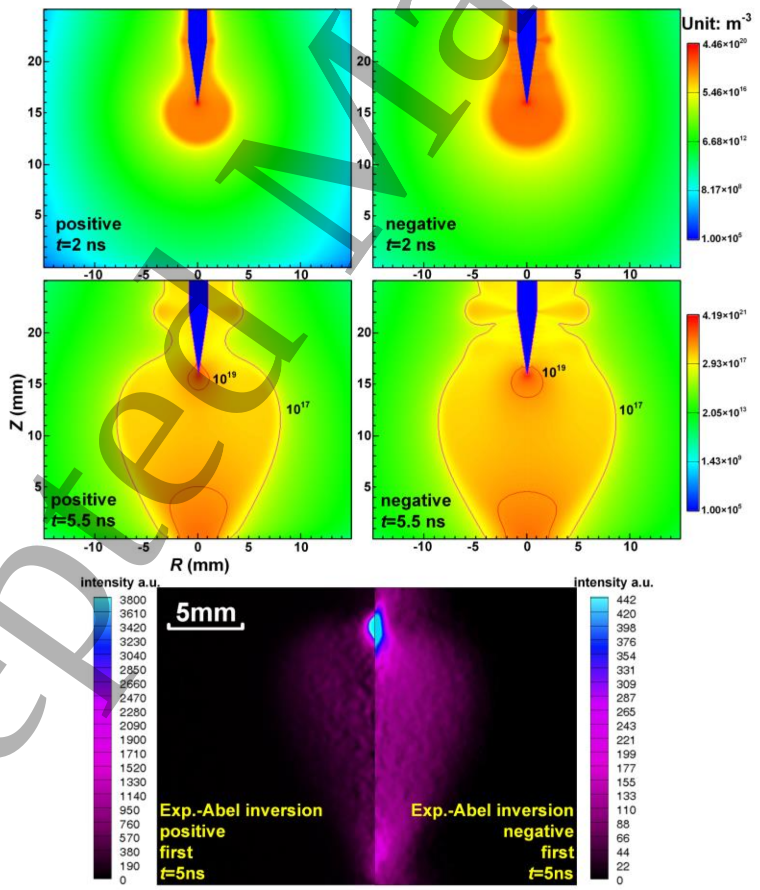

Fig. 16 The $N_2(C^3\Pi_u)$ density distribution in the 20% mixture during the positive and negative discharge. The third row is the discharge image after Abel inversion transform in the

experiment (2ns gate, no accumulation used).

To further study the light emission intensity differences between positive and negative polarities, we use the raw camera data (without normalization) and perform Abel inversion transform, as shown in Fig. 16, to obtain local light intensity instead of spatially integrated intensity Fig. 17 presents the comparison between experimental and simulation results. Both show that the maximum light emission intensity at the pin is lower for negative polarity than for positive polarity. The simulation yields a negative-to-positive maximum intensity ratio of 0.43, whereas the experiment shows a ratio of 0.12. This difference may be due to the experimental result being time-integrated over 2 ns, while the simulation provides an instantaneous value at 5.5 ns.

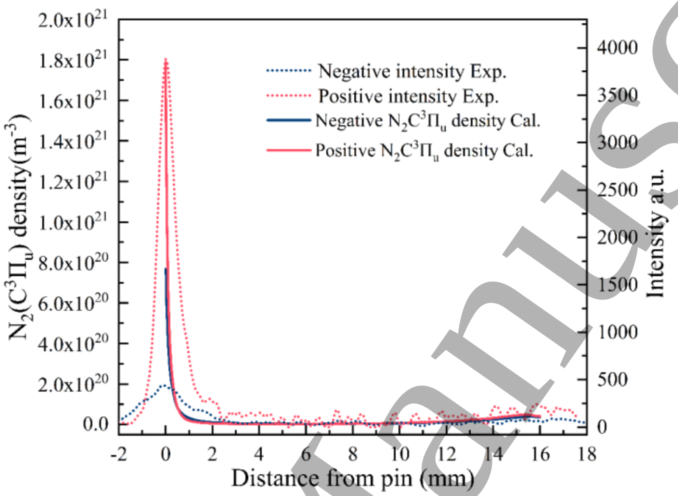

Fig. 17 The $N_2(C^3\Pi_u)$ density on the axis in the simulation and the light emission intensity on the axis after Abel inversion transform in the experiment, for positive (red) and negative (blue) polarities. The dashed lines are extracted from Fig. 16, row three, while the solid lines are extracted from Fig. 16, row two.

4.2 Discussion on the second discharge:

Before discussing the second discharge, the differences in double-pulse discharge modes between diffuse ionization waves and positive streamers must be distinguished. Firstly, both are generated under comparable gas pressures and voltages. In the work of Nijdam *et al* [21], the operating gas pressure is 67-533 mbar, the voltage amplitude is 7-17 kV, the rise time is 15 ns (pulse width over 200 ns), and the electrode gap is 103 mm. Therefore, the streamers in their first discharge appear filamentary and have multiple branches. In their second discharge, as reviewed previously, different development modes occur: the second discharge after a few microseconds propagates along the edge of the first discharge, while the second discharge after several hundred microseconds propagates along the channel of the preceding streamer, and the second discharge after a few milliseconds develops entirely different branches from the previous discharge channel. In contrast to the propagation modes of these positive streamers, diffuse ionization waves in short gaps exhibit a uniform and stable discharge morphology, always appearing with an approximately conical shape below the pin electrode. In the double-pulse mode under positive polarity, the second discharge still develops with the same morphology due to the high pre-ionization level generated by the first discharge, and does not develop along the edge of the previous discharge as filamentary streamers do. Furthermore, at different pulse intervals (20 μs-10 ms), the morphology of the second discharge remains the same as the first and exhibits good symmetry. However, the reduction in the maximum discharge width still shows that the second discharge consistently develops within the ‘body’ of the first discharge until the pulse interval exceeds several milliseconds. In the negative polarity, the second discharge does not exhibit development mode similar to filamentary streamers; instead, it directly produces branching. As shown in the overlapped image in Fig. 18, it shows that the development of the second discharge is entirely different from the first. Considering that Nijdam’s work attributes the behavior of the second filamentary streamer to residual charges, this completely different development mode also implies that factors beyond residual charges are at play.

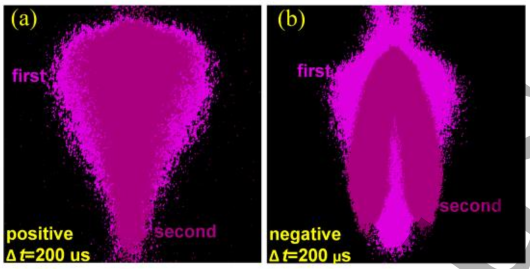

Fig. 18 Overlaping the first and second discharge images in the diffusive ionization wave. (a) is the positive diffusive ionization wave, (b) is the negative one. The light purple one represents the first discharge and the dark purple one represents the second discharge.

4.2.1 Second positive discharge

For the positive discharge, the propagation speed doesn’t change a lot while the discharge width shrinks at the second discharge, showing that the background ionization generated by the first discharge shields the second discharge and makes more concentrated.

To investigate the mentioned phenomena, we conduct fully resolved numerical simulations in two consecutive pulsed discharges. Here we take Δt= 20 μs to show the shielding effect on the second discharge. The electron density in the gap decreases to ~10^{15} m^{-3} after 20 μs. The electron density distribution of the second discharge is shown in Fig. 19, in which the red contour line represents the morphology of the first discharge and the black line represents the second discharge. Compared to the first discharge, the maximum width of the second discharge shrinks from 16.8 mm to 13.2 mm after 20 μs Δt.

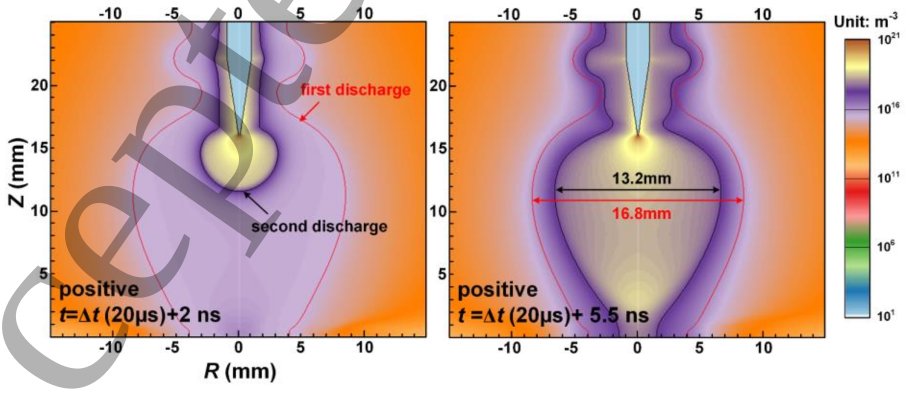

Fig. 19 The ‘shielding effect’ in electron density distribution in the 20% mixture during the second positive discharge. For more obvious contrast, a more contrasting color bar is used.

4.2.2 Second negative discharge

For the negative discharge, the second discharge has a certain probability of branching. Experiment results(see Fig. 11) also show that the branching of negative second discharge starts at the very beginning of the discharge. Besides, the branching probability varies with the pulse interval, indicating that the cause of the instability is strongly time-related. Thus, the cause of the branching phenomenon in negative discharge could be:

- The residual charge left over during the afterglow of the first discharge .
- Leftover metastables or NO generated during the pulse interval lower the ionization threshold for the second discharge.
- The first discharge may cause the gas temperature to rise.
- The first discharge may have generated a shock wave, which created an uneven gas density distribution.

The direct simulated results of the negative discharge differ significantly from the experimental results. As shown in Fig. 20, instead of branching, the second discharge remains diffusive after 20 μs. This is not unexpected, as 20 μs is a rather long time for the residual charge diffusion process to create a uniform and diffusive ionization background, also indicating that the residual charge distribution may not be a key factor in this branching process. Ideally, to better simulate the branching phenomenon of the second discharge, a three-dimensional model that takes into account all the above factors is needed. However, due to the computational resources, this is almost impossible.

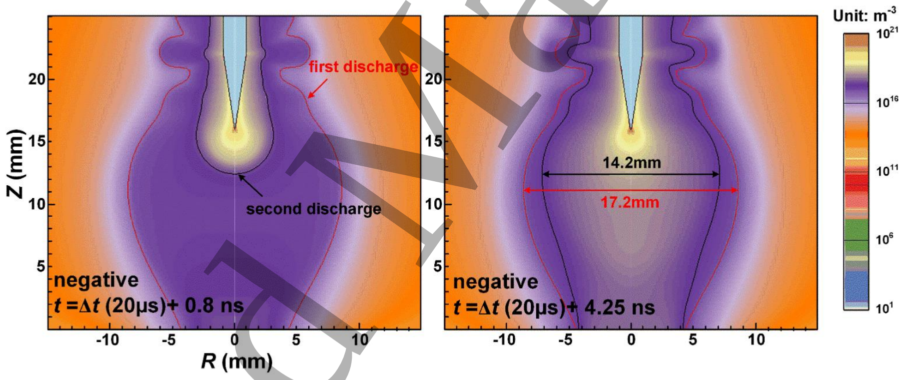

Fig. 20 The electron density distribution in the 20% mixture during the second negative discharge. For more obvious contrast, a more contrasting color bar is used.

It is commonly recognized that negative streamers do NOT need photoionization to propagate, and the growth of local protrusion on the streamer front is likely to destabilize the steamer, which is the basic understanding of Laplacian instability [42-44]. But in this case, when the second discharge branches (for example, in 20% mixture in Fig. 11), not only there is still sufficient electron background for the discharge to maintain its shape (200 μs after the first discharge), but also the discharge channel after the first one is diffusive instead of leaving a on-uniform plasma patch to guide or force the discharge in other different directions. In light of this somewhat counterintuitive phenomenon, we will delve into the underlying causes of discharge destabilization in the following discussion through a combination of simulation and experimental methods.

1) The destabilization of the second discharge: residual charge

In our previous work, through a 3D fluid model, we proved only that high-density (10^{16}-

10^{18} m^{-3}) electro-positive or electro-negative plasma patches can change the propagation path of the negative streamer and make it branch, whereas neutral plasma does not influence its path [20], and it is consistent with the results obtained through PIC/MCC simulations in [19].

As for the double-pulse experiment in this work, a pulse interval of 20 μs or 200 μs is long enough to reduce the density of electrons and ions through electron attachment, electron-ion recombination, ion conversion reactions, and ion-ion recombination. Furthermore, the diffusion of charged species allows the gap to exhibit a quasi-neutral state instead of being electro-negative or electro-positive before the second discharge incepts. This is also verified through the 2D model in this work: the residual net charge density (including all positive and negative charged species) after 200 μs in 20% mixture is shown in Fig. 21. At the end of the first pulse, the net charge near the pin remains at a high negative value, but the main discharge region exhibits a uniform quasi-neutral state with a value between 10^{15}-10^{16} m^{-3}. The distribution becomes more homogeneous after 200 μs except for the very left and right discharge boundaries. The residual charge density in the gap is between 10^{10}-10^{12} m^{-3} in the gap, which is far too low to cause significant changes in discharge propagation direction. Thus, in this case, the potential formation of electro-negative or electro-positive residual charge is not likely to cause the negative discharge to branch at the second pulse.

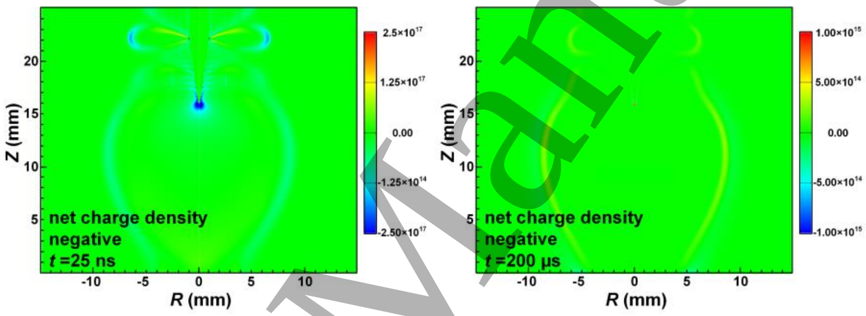

Fig. 21 The distribution of residual net charge density after 25 ns (the first pulse) and 200 μs pulse interval in negative discharge.

Furthermore, as demonstrated by the results in the work of Babaeva and Naidis [45], non-uniform seed electron distributions can induce streamer branching. A similar seed electron distribution set is used to test the negative diffusive ionization wave, and the electron density distribution results are shown in Fig. 22. For ionization waves with a larger area than filamentary streamers, they are not affected by the non-uniformly distributed seed electrons. Instead, they directly pass this seed distribution area, and the seed electrons are compressed under the influence of the ionization wave head. This result indicates that, unlike the findings in the double-pulse work of Nijdam et al [21], residual electrons do not significantly influence diffuse ionization wave path.

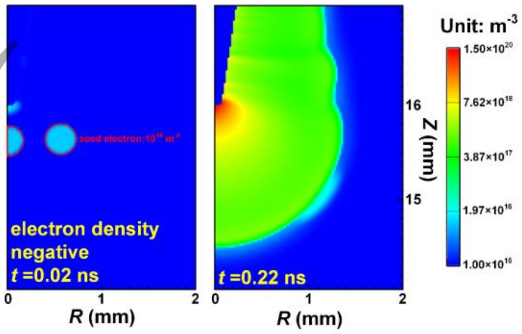

Fig. 22 Electron density distribution during the development of negative ionization wave under a non-uniform seed electron distribution.

2) The destabilization of the second discharge: leftover paritcles

Based on the above assumption, we add the following electron-production reactions involving meatastables and NO-related reactions to the original reaction system shown in Appendix A.

Table 1. Reactions for the production of certain metastable species and electrons.

	Reaction	Rate Constant*	Ref
R1-1	$e+O_2 \rightarrow O(^3P)+O(^3P)$	$f(\varepsilon)$	[46]
R1-2	$e+O_2 \rightarrow O(^3P)+O(^1D)$	$f(\varepsilon)$	[46]
R1-3	$e+O_2 \rightarrow O(^3P)+O(^1S)$	$f(\varepsilon)$	[46]
R1-4	$e+O_2 \rightarrow e+O_2^*(b)$	$f(\varepsilon)$	[46]
R1-5	$O_2^-+O_2^*(b) \rightarrow e+O_2$	$1.24\times10^{-11}\exp((-179/(E/N+8.8))^2)$	[47]
R1-6	$O_2^-+N_2^*(A) \rightarrow e+O_2+N_2$	2.10×10^{-9}	[47]
R1-7	$O_2^-+O(^3P) \rightarrow e+O_3$	1.50×10^{-10}	[47]
R1-8	$O_3^-+O(^3P) \rightarrow e+2O_2$	3.00×10^{-10}	[47]

Table 2. Reactions involving NO.

	Reaction	Rate Constant*	Ref
R2-1	$e+NO+M \rightarrow NO^-+M$	10^{-30}	[47]
R2-2	$e+NO \rightarrow e+e+NO^+$	$f(\varepsilon)$	[48]
R2-3	$O^-+N \rightarrow e+NO$	2.60×10^{-10}	[47]
R2-4	$N_2^++O_2 \rightarrow NO^++NO$	1.00×10^{-17}	[47]
R2-5	$N_2^++O(^3P) \rightarrow NO^++N$	$1.30\times10^{-10}(300/T_{gas})^{0.5}$	[47]
R2-6	$N_2^++NO \rightarrow NO^++N_2$	3.30×10^{-10}	[47]
R2-7	$N_4^++NO \rightarrow NO^++2N_2$	4.00×10^{-10}	[47]
R2-8	$O_2^++N_2 \rightarrow NO^++NO$	1.00×10^{-17}	[47]
R2-9	$O_2^++N \rightarrow NO^++O(^3P)$	1.20×10^{-10}	[47]
R2-10	$O_2^++NO \rightarrow NO^++O_2$	4.40×10^{-10}	[47]
R2-11	$O_4^++NO \rightarrow NO^++2O_2$	1.00×10^{-10}	[47]

*Unit of rate constants are s^{-1}, $cm^3\cdot s^{-1}$, and $cm^6\cdot s^{-1}$. T_{gas} is the gas temperature, units in K. T_e is the electron temperature, units in K.

Fig. 23 shows the temporal evolution of electron source terms from different reactions and the densities of various species at Z=15.5 mm during the 'pulse-off' period, obtained from simulations after adding the above reactions to the original reaction system. In terms of electron production rate, detachment reactions involving $O(^3P)$ contribute the largest proportion of electron source terms. Regarding species density, as the pulse interval increases, all shown species densities show a decreasing trend.

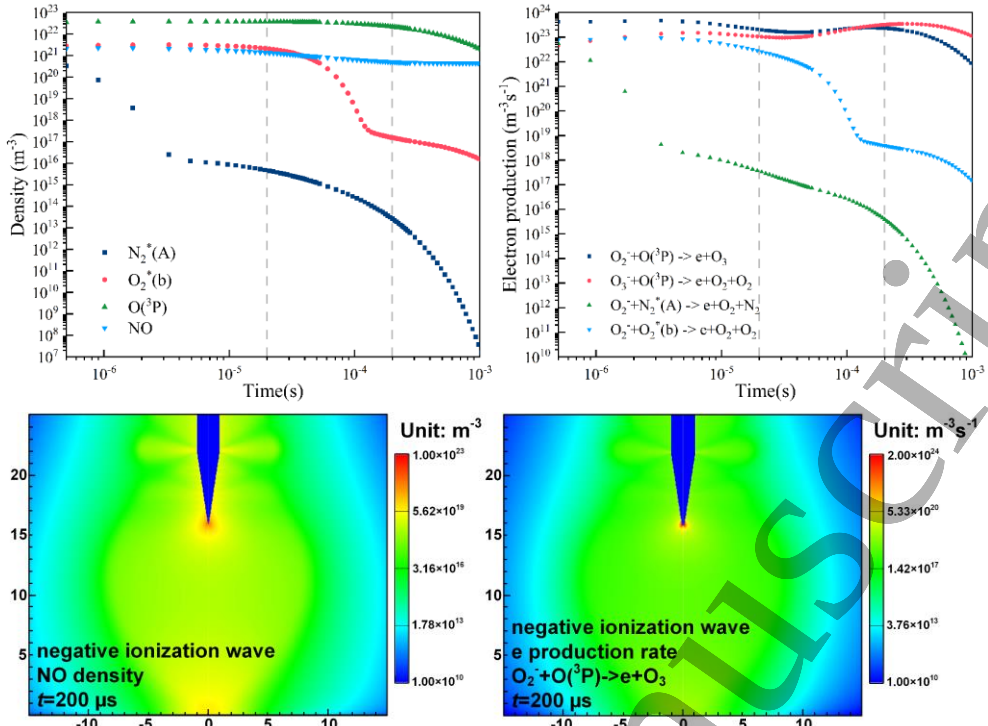

Fig. 23 Densities of selected species and electron source terms from major contributing reactions during the pulse interval in the 20% gas mixture, after new reactions are added to the original reaction system. The first row shows the temporal evolution at *Z*=15.5mm throughout the pulse interval. The second row shows the 2D distribution after a Δ*t*=200 μs.

After adding above reactions, the electron density of the second discharge after a Δ*t*=20 μs is shown in Fig. 24. The negative ionization wave still maintains a diffusive shape, but its development velocity is slightly faster compared to the case without these additions: at *t*=(20 μs+) 0.8 ns, the propagation position after adding the new reactions leads the original by 0.25 mm. However, branching is still not observed. This suggests that within the chosen reaction system, these are not the causes of negative ionization wave branching.

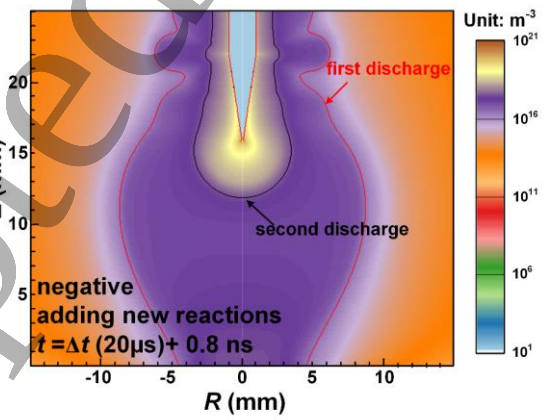

Fig. 24 Electron density distribution after new reactions are introduced.

Why is branching still not observed even after introducing species with lower ionization degrees? One of the major reasons we believe lies in inhomogeneity: spatial inhomogeneity is the primary factor for introducing Laplacian instability in negative polarity discharges. However, even with a more complete reaction system, existing 2D axisymmetric fluid models still lack the inhomogeneity caused by stochasticity. To fully simulate branching behavior, introducing stochastic ionization or employing a 3D model might be more appropriate. Or, as in [49], if one artificially introduces high-density positive charges on the symmetry axis, only then can this homogeneity in 2D axisymmetric fluid models be broken, thereby forcing the discharge to branch and deviate from the symmetry axis.

3) The destabilization of the second discharge: gas temperature

Gas heating could also be an important factor in changing the streamer characteristics, and even further can cause the discharge mode transition to higher ionization degree like sparks. In high-temperature gases, steamers near the anode could become thinner [39], which may further cause streamer branch. However, according to the work of Ono *et al* [50], this only becomes very obvious when the gas temperature is very high (over 1000 K). Through optical emission spectroscopy, we tried to measure the rotational temperature of N2(C) excited state of molecular nitrogen after the negative diffusive ionization wave bridges the two electrodes at 5 ns in the 20% mixture, which is considered to be equivalent to the gas temperature in non-equilibrium plasmas. A typical experiment and calculated rotational N_2(C-B)(0-0) spectrum through SPECAIR software [51] is shown in Fig. 25(a). We use the same measurement method as in [52]. The results of the measured gas temperature are shown in Fig. 25(b). The maximum gas temperature near the pin electrode of the first pulse measured is around 350 K, and around 370 K for the second discharge, showing the gas temperature rise is rather low. Besides, we also conducted OES measurement for the inception cloud in Section 3.5, and the gas temperature at the pin remains 300 K in all the experiments, which aligns with fundamental physical intuition.

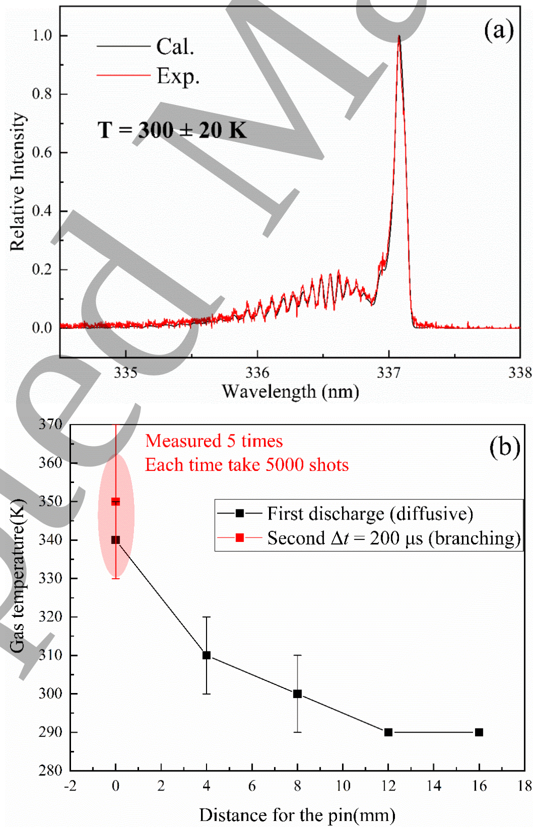

Fig. 25 The OES measurement results at 5 ns after the discharge inception in the 20% gas mixture. (a) is the calculated and experiment spectrum at around 300 K. (b) is the measured gas temperature results on the axis, and each point is the result of 5000 shots. Note that in (b)

the error bar is the results of 5 measuring times, and there is still a fixed error of 20 K for the calculation-experiment fitting that is not reflected in this figure.

In the simulation, the gas temperature after the first discharge is also calculated as shown in Fig. 26. For the diffusive ionization wave, at the location where the second discharge initiates branching (Z=15.3 mm), the gas temperature at t=40 ns is 325 K. Similarly, for the inception cloud, at the corresponding branching location (Z=158 mm), the gas temperature at t=40 ns is 300 K. The simulation shows a limited gas temperature increase after one complete discharge, aligning qualitatively with experimental observations. Importantly, the simulation provides the temperature after the first pulse, whereas the experiment measures it only during light emission from both pulses. Therefore, the temperature behavior during the pulse inverval phase caused by the energy transfer to neutrals from vibrationally excited molecular nitrogen metastables produced during the discharge, which is much slower than the fast gas heating process, remains unresolved by these approaches.

Accurate determination of gas temperature in the discharge afterglow via spontaneous Raman scattering is demonstrated by studies such as those by Brisset *et al* [53], who observed the $N_2(X,v)$ rotational temperature near the pin (1.5 mm) in an atmospheric-pressure diffuse discharge peaking at ~1200 K around 100 μs before decreasing. In the work of Montello *et al* [54, 55], they found that this temperature rises from 300K after the discharge to ~700 K after 1ms, and then decreases back to 300 K after 10 ms in a low-pressure (100 Torr) air pin-to-pin discharge. Therefore, an increase in rotational temperature during the pulse interval remains expected in this work. This could potentially generate a hydrodynamic shock front, which, as pointed out by Nijdam *et al* [39], can subsequently create macroscopic perturbations at the discharge head, thereby inducing discharge branching.

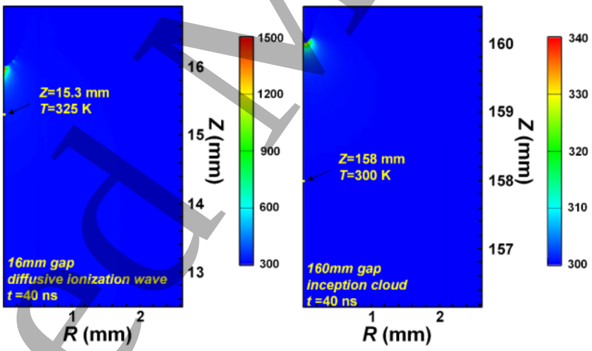

Fig. 26 The gas temperature in simulation after 40 ns.

4) The destabilization of the second discharge: gas density gradient

Pulsed discharges like streamers, sparks, and arcs can generate shockwaves and lead to local variations in gas density, and further change discharge characteristics[56]. Starikovskiy *et al* [57] proved that streamer characteristics including shape change significantly when encountering sharp gas density gradients. Due to the delayed energy transfer, a shockwave is often generated after the discharge and propagates. Ono *et al* [58] observed that it takes several microseconds for the shockwave to be generated after a steamer discharge at atmospheric pressure. In this work, we simulate the changes in gas pressure and relative gas density during the pulse interval in our experiment are shown in Fig. 27. During the pulse interval calculation, we save computational resources and time by freezing the electric field at Δt=500 ns(max E/N≈12 Td, long after the first pulse ended at 25 ns) and calculating plasma reactions and Euler equations between

Δt=500 ns and Δt=200 μs, while concurrently employing a coarser grid (gradually transitioning from a plasma grid of 5 μm to a 200 μm grid for gas pressure and density calculations) compared to that used for high-density plasma.

As depicted in the figure, identical time points and color scales for both positive and negative ionization waves are used. Therefore, the directly observable differences in the figure represent distinctions in their calculated results. Regarding shock wave propagation speed, it propagates slightly faster in the negative polarity than that in the positive polarity, 384 m/s and 367 m/s, respectively, slightly exceeding the speed of sound in air. Moreover, their shock wave generation processes are nearly identical: initially, a spherical shape forms near the pin, which then collectively forms a shock wave with the gas below the pin, and propagates outwards, with their shapes also being almost identical. However, distinct differences emerge in their quantitative values. For the gas pressure at the shock wave front, negative polarity exhibits significantly higher values than positive polarity, a distinction particularly pronounced within the first 20 μs. For example, at 5 μs, the negative polarity shock wave front is approximately 790 Pa higher than positive polarity, and at 20 μs, it is 200 Pa higher. More crucially than the shock wave front, the gas density below the pin serves as a vital factor influencing the second discharge. Assuming an initial gas density of 1 for the 20% mixture at 200 mbar before discharge, the gas density evolution during the pulse interval is depicted in the second and fourth rows of the figure. For negative polarity, the gas density beneath the needle tip is considerably lower than that for positive polarity. Using Z=15.5 mm as a reference point, at 5 μs, the negative polarity gas density is 0.61, while positive polarity is 0.80. At 20 μs, the negative polarity gas density is 0.84, and positive polarity is 0.92. Even at 200 μs, despite Fig. 27 indicating a seemingly uniform gas density under the same color scale, subtle differences persist. Specifically, as illustrated in Fig. 28, the positive polarity value is still higher than that for negative polarity. In summary, these simulation results indicate that a notable difference in gas density between positive and negative polarities persists within 200 μs, and the area of the low-density region under negative polarity is greater than that under positive. This disparity is more pronounced at 20 μs compared to 200 μs and is expected to have a greater impact on the branching process.

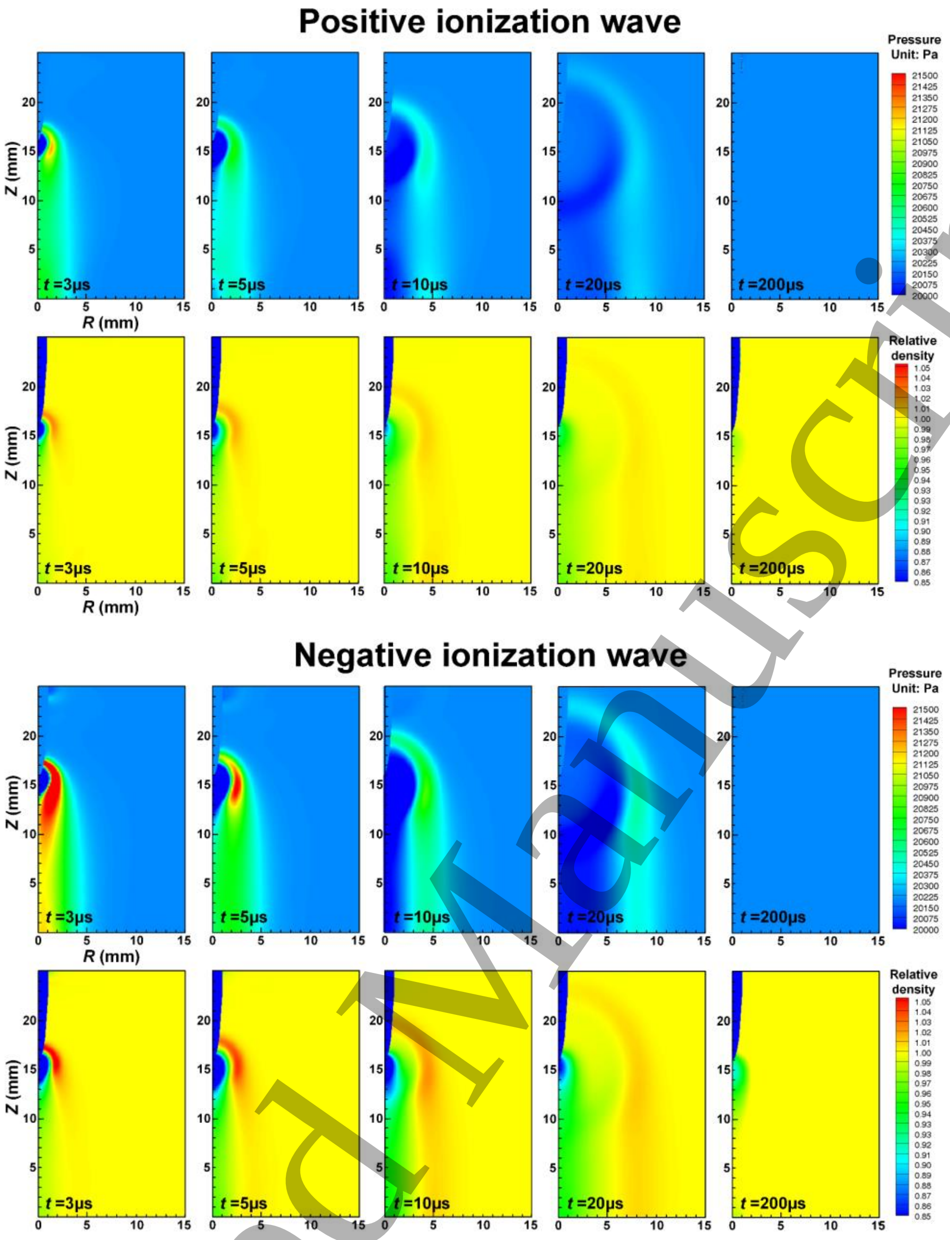

Fig. 27 Simulated temporal evolution of gas pressure and gas density during positive and negative polarity ionization waves development.

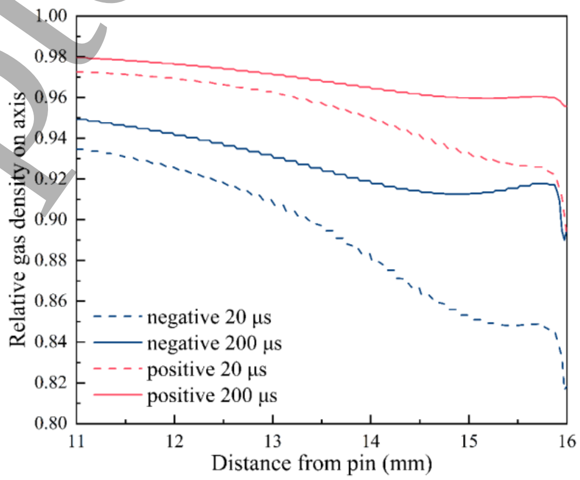

Fig. 28 Axial gas density distribution for positive and negative polarity ionization waves at 20 μs and 200 μs.

Using a classic Z-Fold Schlieren, the schlieren images of the 20% gas mixture are obtained as shown in Fig. 29. By adjusting the contrast, the stripes in the figure become more prominent. These images capture the positive and negative polarity ionization waves at Δt=3μs using a high-speed camera. After this time, images with good contrast cannot be captured. This means that, as shown in the simulation results, the gas density change at the shock wave front after this moment is too small to be displayed by the existing system. Although these schlieren images have low contrast due to the small gas density change, the negative polarity generally shows better contrast than the positive polarity, allowing for a qualitative judgment that the gas density change at the shock wave front is greater and faster. Yet due to the poor contrast, the low-density region below the pin is not clearly discernible.

It should be noted that in this Z-fold schlieren system composed of two concave mirrors, the collimated light path first passes through the atmosphere after passing through the first concave mirror, then passes through the experimental chamber (200 mbar internally), then passes through the atmosphere again, and finally reaches the second concave mirror. This means that when measuring low-pressure schlieren images, the atmospheric environment introduces a ‘baseline’ that reduces the accuracy of measurements. Therefore, these images can only provide a qualitative reference.

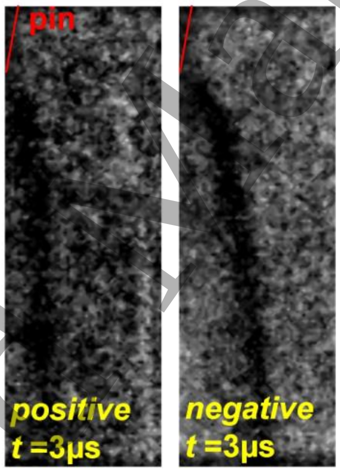

Fig. 29 Schlieren images of the 20% gas mixture obtained using a Z-Fold Schlieren set-up. The camera gate width is 500 ns, and the capture time is 3 μs after the end of the first discharge.

Thus, in our case, it is likely that when the second discharge incepts, it happens to reaches the low-density/high density surface below the pin formed by the first discharge then a protrusion is created and starts to grow, as shown in the schematic diagram in Fig. 30.

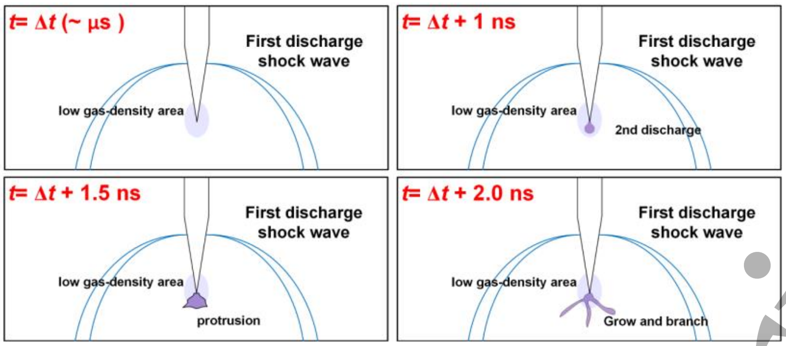

Fig. 30 Schematic diagram of the hypothesized cause for negative polarity discharge branching. In the figure, blue lines represent the shock wave front, the light blue area represents the low-density region, and dark purple represents the second discharge.

In the work of Guo *et al* [59], they used a 3D fluid model to investigate positive streamer characteristics under the influence of different gas gradient types: positive streamers tend to branch at boundaries with large gas density gradients and propagate along these interfaces. To prove the assumption that the gas gradient surface generated by the former discharge could make the subsequent negative discharge branch, we then import the gas density distribution at Δt=20 μs as the initial condition for calculating the second discharge, and to simplify the calculation process and ensure computational accuracy during the mesh transition between the interval and the discharge, we average the gas density in the low-density region. The simulation set-up used is shown in Fig. 31. The light blue area represents the low-density region (density n_1), and the orange region represents the normal gas density region (density n_0=4.88×10^{24}m^{-3}).

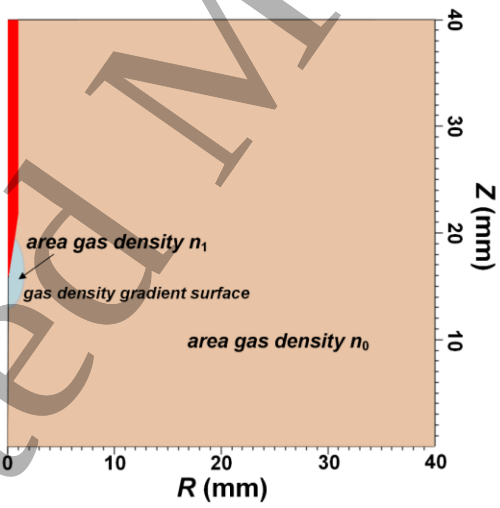

Fig. 31 The new set for the 2D axisymmetric model: different gas density is set in two areas to create a gas density gradient surface.

The electric field obtained from simulations with n_1/n_0=0.92 for positive polarity and n_1/n_0 = 0.84 for negative polarity, before and after the ionization wave crosses the gas gradient surface, are shown in Fig. 32. Due to the use of different gas densities, the unit of electric field strength in the figure is kV/cm. For the positive polarity, the electric field at ionization wave head does not show significant protrusion before and after crossing this surface; the electric field distribution at the head remains relatively smooth, mainly due to the small gas density gradient. In contrast, the negative polarity exhibits a greater protrusion after the crossing. Similar to the schematic diagram, the electric field at the head develops a clearly uneven distribution, thus having a probability of growing to branch during further development. There is also a significant difference in the electric field at the head of the diffusive ionization waves between positive and negative polarities. The electric field at the head of the positive polarity is approximately 15 kV/cm higher than that of the negative polarity (second column in Fig. 32). This also implies that the negative polarity has a weaker ability to 'resist' the electric field changes caused by the gas density gradient, meaning it is more easily influenced by the gas gradient surface. As the ionization wave develops, the negative ionization wave 'separates' a branched streamer from the main discharge channel on the axis (third column in Fig. 32), but it develops more slowly compared to the main discharge channel. Combining the results from both positive and negative discharges, this illustrates that the gas density gradient near the pin causes the branching process.

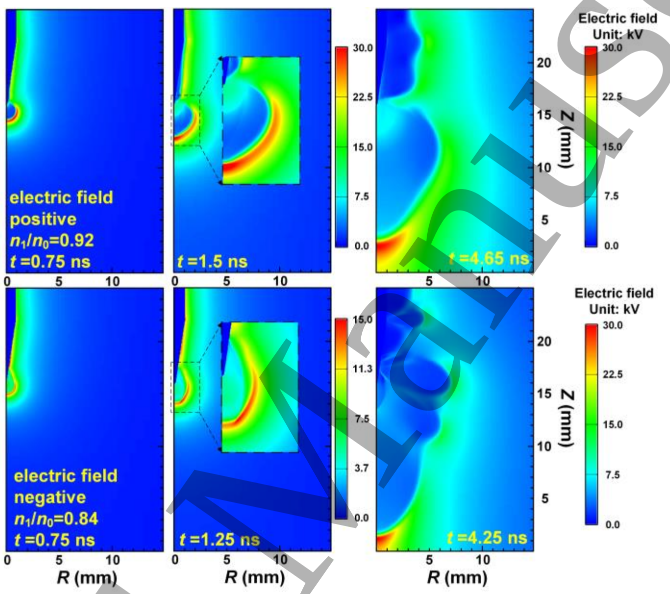

Fig. 32 Changes in electric field distribution of positive and negative polarity ionization waves as they cross different gas density gradient surfaces.

However, these simulation results can only explain the reason for branching of the negative ionization wave after Δt=20-200 μs. As energy relaxation goes, the branching probability remains high at Δt=1 ms, when the gas density in the gap has likely become uniformly distributed. Nevertheless, a small gas density gradient may still exist near the pin. As shown by the schlieren experiments of Komuro *et al* [60], in atmospheric pressure air, filamentary streamer discharges generated by a -15 kV voltage applied across a 13 mm electrode gap still leave a significant gas density gradient near the pin 1-10 ms after the discharge. However, due to the need to upgrade the existing schlieren measurement system for better results in low-pressure environments, the explanation for the branching phenomenon remains speculative.

Futher, when discussing the differences between positive and negative discharges, it is crucial to consider their head structures. Positive streamer heads are generally more focused, possessing a smaller radius of curvature, whereas negative ones are the opposite. Furthermore, unlike negative streamers, the region ahead of the positive streamer space charge layer can possess an additional 'active zone' filled with electrons sustained by background ionization and photoionization [39]. This active zone can suppress the potential growth of protrusions induced by Laplacian instability or other instabilities, thereby maintaining the stability of its head. In contrast, as discussed in [42], negative streamer tends to destabilize even within deterministic fluid models. This might also be one of the reasons why, in this work, negative polarity is more prone to branching than positive polarity.

5. Conclusions

In this work, we experimentally studied both positive and negative diffusive ionization wave characteristics under a double voltage pulse scheme in different oxygen concentration mixtures and discussed several unique branching phenomena through a 2D axisymmetric fluid model.

For the single pulsed discharge (or the first discharge), positive ionization wave width and length slightly decrease with the oxygen concentration, yet the negative ionization wave characteristics are very much alike in different mixtures.

For the double-pulse scheme, the positive ionization wave shrinks but propagates with the same velocity compared to the first discharge due to the shielding effect, which is reproduced with a 2D model in Section 4.2.1. But for the negative discharge, it is observed that the second discharge has a certain probability of branching, and this probability first increases and then decreases with the pulse interval Δt. This particular phenomenon occurs in all the tested gas mixtures and in the inception cloud in a 160 mm gap.

Through a combined method of measurement and simulation on full double-pulse including pulse interval, we exclude residual charge effects and gas temperature as dominant contributors to the branching phenomenon. Thourgh modeling on the gas density during the pulse interval, we attribute the branching reason to shock wave-induced gas density gradients near the pin electrode generated by the first discharge. When the second discharge cross the gradient surface, localized protrusions will be created and start to grow into filament streamers. The negative polarity's electric field head is lower than the positive polarity's in the second discharge, suggesting a reduced capacity to resist branching due to gas density inhomogeneity. Furthermore, the observed reduction in discharge branching probability may be attributed to the decreasing gas density gradient near the pin over time.

However, there are several questions remain unresolved:

1. Capturing the gas density changes in low-pressure environments with the current schlieren system is challenging, and transient processes are difficult to capture, especially the gas density changes near the pin. It may be necessary to employ alternative methods to obtain images with higher contrast to validate the accuracy of the simulation results.

2. The experimental results show that negative diffuse ionization waves still have a high probability of branching 1 ms after the first discharge ends. What is the gas density gradient near the pin at this time? While some literature at atmospheric pressure indicates a significant gas density gradient remains, the specific values in this low-pressure case still need to be measured. Further evaluation of its impact on branching is also required.

Future investigations employing a three-dimensional model, currently under development, that explicitly incorporates discharge energy relaxation and shock wave generation are expected to accurately capture both observed discharge behaviors, thereby providing a more comprehensive understanding of the underlying mechanisms.

Acknowledgments

Project supported by the China Scholarship Council (CSC) (Grant No. 202206280081), the Natural Science Basic Research Program of Shaanxi (No. 2024ZY-JCYJ-01-06), the National Natural Science Foundation of China (Grant No. 52077169), the Fundamental Research Funds for the Central Universities, China (Grant No. xtr052023003, xpt012024063), and the State Key Laboratory of Electrical Insulation and Power Equipment, China (Grant No. EIPE23114). The authors would also like to thank E. Marode for his valuable suggestions. We would also like to thank the anonymous referees for their valuable suggestions.

Data availability statement

The data that support the findings of this study are available upon reasonable request from the authors.

Appendix A. Reactions in the 2D model

Table A1. Reactions considered in the 2D fluid model

	Reaction	Rate Constant*	Ref
R1	$e+N_2 \rightarrow N_2^+ +e+e$	$f(\sigma, \varepsilon)$	[61]
R2	$e+O_2 \rightarrow O_2^+ +e+e$	$f(\sigma, \varepsilon)$	[62]
R3	$e+O_2+O_2 \rightarrow O_2^- +O_2$	$f(\varepsilon)$	[62]
R4	$e+O_2 \rightarrow O^- +O$	$f(\varepsilon)$	[62]
R5	$O_2^- +M \rightarrow e+ O_2+M$	$f(\varepsilon)$	[63]
R6	$O^- + N_2 \rightarrow e+N_2O$	$f(\varepsilon)$	[63]
R7	$O^- + O_2 \rightarrow O_2^- + O$	$f(\varepsilon)$	[63]
R8	$O^- + O_2+M \rightarrow O_3^- +M$	$f(\varepsilon)$	[63]
R9	$N_2^+ +O_2 \rightarrow O_2^+ +N_2$	$6\times10^{-11}\times(300/T_{gas})^{0.5}$	[47]
R10	$N_2^+ +N_2+M \rightarrow N_4^+ +M$	$5\times10^{-29}\times(300/T_{gas})^{2}$	[47]
R11	$N_4^+ + O_2 \rightarrow O_2^+ +N_2+N_2$	2.5×10^{-10}	[47]
R12	$O_2^+ + O_2+M \rightarrow O_4^+ + M$	$2.4\times10^{-30}\times(300/T_{gas})^{3}$	[47]
R13	$O_2^+ +N_2+N_2 \rightarrow O_2^+N_2+N_2$	9×10^{-31}	[47]
R14	$O_2^+N_2+N_2 \rightarrow O_2^+ +N_2+N_2$	4.3×10^{-10}	[47]
R15	$O_2^+N2+O_2 \rightarrow O_4^+ +N_2$	1×10^{-9}	[47]
R16	$e+N_4^+ \rightarrow N_2+N_2$	$2\times10^{-6}\times(300/T_{gas})^{0.5}$	[47]
R17	$e+O_4^+ \rightarrow O_2+ O_2$	$1.4\times10^{-6}\times(300/T_{gas})^{0.5}$	[47]
R18	$N_2^+ + O^- \rightarrow N+N+O$	10^{-7}	[47]
R19	$N_2^+ +O_2^- \rightarrow N+N+ O_2$	10^{-7}	[47]
R20	$N_2^+ +O_3^- \rightarrow N+N+ O_3$	10^{-7}	[47]
R21	$O_2^+ + O^- \rightarrow O+O+O$	10^{-7}	[47]
R22	$O_2^+ +O_2^- \rightarrow O+O+ O_2$	10^{-7}	[47]
R23	$O_2^+ +O_3^- \rightarrow O+O+ O_3$	10^{-7}	[47]
R24	$O_4^+ + O^- \rightarrow O_2+ O_2+O$	10^{-7}	[47]
R25	$O_4^+ +O_2^- \rightarrow O_2+ O_2+ O_2$	10^{-7}	[47]

R26	$O_4^+ + O_3^- \rightarrow O_2 + O_2 + O_3$	10^{-7}	[47]
R27	$N_4^+ + O^- \rightarrow N_2 + N_2 + O$	10^{-7}	[47]
R28	$N_4^+ + O_2^- \rightarrow N_2 + N_2 + O_2$	10^{-7}	[47]
R29	$N_4^+ + O_3^- \rightarrow N_2 + N_2 + O_3$	10^{-7}	[47]
R30	$N_2^+ + O^- + M \rightarrow N_2O + M$	$2\times10^{-25}\times(300/T_{gas})^{2.5}$	[47]
R31	$N_2^+ + O^- + M \rightarrow N_2 + O + M$	$2\times10^{-25}\times(300/T_{gas})^{2.5}$	[47]
R32	$N_2^+ + O^- \rightarrow N_2 + O$	$2\times10^{-7}\times(300/T_{gas})^{0.5}$	[47]
R33	$N_2^+ + O_2^- + M \rightarrow N_2 + O_2 + M$	$2\times10^{-25}\times(300/T_{gas})^{2.5}$	[47]
R34	$N_2^+ + O_2^- \rightarrow N_2 + O_2$	$2\times10^{-7}\times(300/T_{gas})^{0.5}$	[47]
R35	$N_2^+ + O_3^- \rightarrow N_2 + O_3$	$2\times10^{-7}\times(300/T_{gas})^{0.5}$	[47]
R36	$O_2^+ + O^- + M \rightarrow O_3 + M$	$2\times10^{-25}\times(300/T_{gas})^{2.5}$	[47]
R37	$O_2^+ + O^- + M \rightarrow O_2 + O + M$	$2\times10^{-25}\times(300/T_{gas})^{2.5}$	[47]
R38	$O_2^+ + O^- \rightarrow O_2 + O$	$2\times10^{-7}\times(300/T_{gas})^{0.5}$	[47]
R39	$O_2^+ + O_2^- + M \rightarrow O_2 + O_2 + M$	$2\times10^{-25}\times(300/T_{gas})^{2.5}$	[47]
R40	$O_2^+ + O_2^- \rightarrow O_2 + O_2$	$2\times10^{-7}\times(300/T_{gas})^{0.5}$	[47]
R41	$O_2^+ + O_3^- \rightarrow O_2 + O_3$	$2\times10^{-7}\times(300/T_{gas})^{0.5}$	[47]
R42	$e + N_2 \rightarrow e + N_2(A^3\Sigma_u)$	$f(\varepsilon)$	[61]
R43	$e + N_2 \rightarrow e + N_2(B^3\Pi_g)$	$f(\varepsilon)$	[61]
R44	$e + N_2 \rightarrow e + N_2(C^3\Pi_u)$	$f(\varepsilon)$	[61]
R45	$e + O_2 \rightarrow e + O + O$	$f(\varepsilon)$	[62, 64]
R46	$O^- + O \rightarrow O_2 + e$	5×10^{-10}	[47]
R47	$O_2^- + O \rightarrow O_2 + O + e$	1.5×10^{-10}	[47]
R48	$e + N_2^+ \rightarrow N + N$	$2.8\times10^{-7}\times(300/T_e)^{0.5}$	[47]
R49	$e + O_2^+ \rightarrow O + O$	$2\times10^{-7}\times(300/T_e)$	[64, 65]
R50	$N_2(C^3\Pi_u) + N_2 \rightarrow N_2(B^3\Pi_g, v) + N_2$	1×10^{-11}	[64]
R51	$N_2(C^3\Pi_u) + O_2 \rightarrow N_2 + O + O$	3×10^{-10}	[64]
R52	$N_2(C^3\Pi_u) \rightarrow N_2 + h\nu$	2.38×10^{7}	[65]
R53	$N_2(B^3\Pi_g) + O_2 \rightarrow N_2 + O + O$	3×10^{-10}	[64]
R54	$N_2(B^3\Pi_g) + N_2 \rightarrow N_2(A^3\Sigma_u) + N_2(v)$	1×10^{-11}	[64]
R55	$N_2(A^3\Sigma_u) + O_2 \rightarrow N_2 + O + O$	$2.5\times10^{-12}\times(T_{gas}/300)^{0.5}$	[64]
R56	$O + O_2 \rightarrow O + O_2$	$3.3\times10^{-11}\times\exp(67/T_{gas})$	[64]
R57	$O + N_2 \rightarrow O + N_2$	$1.8\times10^{-11}\times\exp(107/T_{gas})$	[64]
R58	$e + O_2^+N_2 \rightarrow N_2 + O_2$	$1.3\times10^{-6}\times\exp(300/T_e)^{0.5}$	[47]
R59	$O_4^+ + N_2 \rightarrow O_2^+N_2 + O_2$	$4.61\times10^{-12}\times(T_{gas}/300)^{2.5}\times\exp(-2650/T_{gas})$	[47]
R60	$O_2^+N_2 + O^- \rightarrow N_2 + O_2 + O$	10^{-7}	[47]
R60	$O_2^+N_2 + O_2^- \rightarrow N_2 + O_2 + O_2$	10^{-7}	[47]
R60	$O_2^+N_2 + O_3^- \rightarrow N_2 + O_2 + O_3$	10^{-7}	[47]

*Unit of rate constants are s^{-1}, $cm^3\cdot s^{-1}$, and $cm^6\cdot s^{-1}$. T_{gas} is the gas temperature, units in K. T_e is the electron temperature, units in K.

Appendix B. Comparison of ionization wave length in simulation and experiment.

The comparison between simulation and experimental results of discharge length under positive and negative polarity in a 20% mixture is shown in Fig. B1. The ionization wave length in the simulation is determined by the position of the maximum electric field on the axis. In the negative polarity, both the simulated and experimental diffuse ionization waves reach the plane electrode at 5 ns. During their development, the simulation develops slightly slower, but due to the poor repeatability of negative polarity, the simulation results still fall within the error bar range of the experimental data.

In the positive polarity, the experimental and simulation results for the first discharge show good agreement in length, and their development speeds are largely consistent. However, the simulation reaches the plane electrode 0.5 ns later than the experiment. For the second discharge with a 20 μs pulse interval, the results differ more significantly from the experiment. Although both reach the plane electrode after 5 ns, the simulation shows a faster development speed during the process.

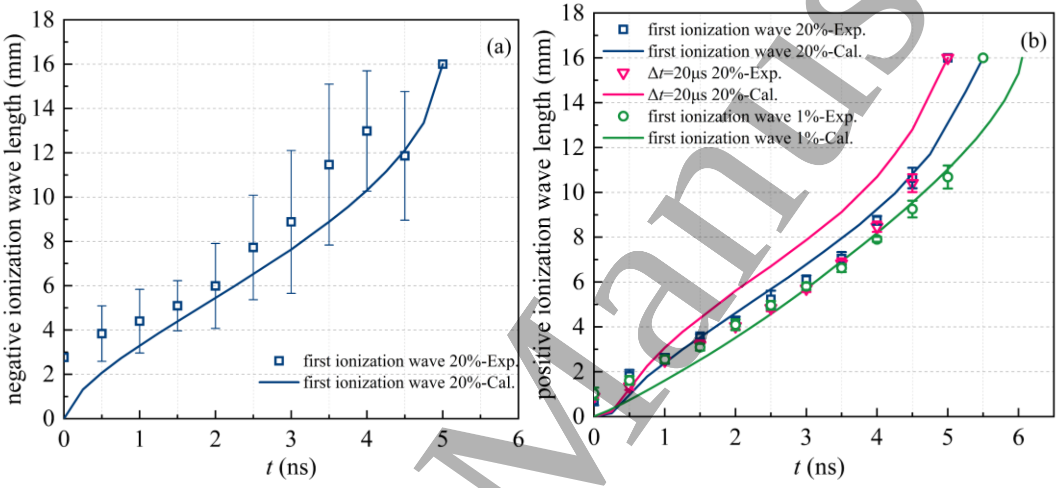

Fig. B1 Comparison of the length of negative and positive ionization wave versus time in experiment and simulation. (a) is the negative ionization wave, (b) is the positive ionization wave.

References

[1] Marode E, Dessante P and Tardiveau P 2016 2D positive streamer modelling in NTP air under extreme pulse fronts. What about runaway electrons? *Plasma Sources Science & Technology* **25** 064004

[2] Tarasenko V 2020 Runaway electrons in diffuse gas discharges *Plasma Sources Science & Technology* **29** 034001

[3] Iza F, Walsh J L and Kong M G 2009 From Submicrosecond- to Nano second-Pulsed Atmospheric-Pressure Plasmas *Ieee Transactions on Plasma Science* **37** 1289-1296

[4] Lu X, Reuter S, Laroussi M and Liu D *Nonequilibrium atmospheric pressure plasma jets: Fundamentals, diagnostics, and medical applications*: CRC Press, 2019

[5] Wu S, Xu H, Lu X and Pan Y 2013 Effect of Pulse Rising Time of Pulse dc Voltage on Atmospheric Pressure Non-Equilibrium Plasma *Plasma Processes and Polymers* **10** 136-140

[6] Shcherbanev S A, Ding C, Starikovskaia M and Popov N A 2019 Filamentary nanosecond surface dielectric barrier discharge. Plasma properties in the filaments *Plasma Sources Science*

& Technology **28** 065013

[7] Qi F, Li Y Y, Zhou R S, Zhou R W, Wan J J, Xian Y B, Cullen P J, Lu X P and Ostrikov K 2019 Uniform atmospheric pressure plasmas in a 7 mm air gap *Applied Physics Letters* **115** 194101

[8] Zhao Z, Huang D D, Wang Y N, Li C J and Li J T 2020 Volume and surface memory effects on evolution of streamer dynamics along gas/solid interface in high-pressure nitrogen under long-term repetitive nanosecond pulses *Plasma Sources Science & Technology* **29** 015016

[9] Höft H, Kettlitz M, Becker M M, Hoder T, Loffhagen D, Brandenburg R and Weltmann K D 2014 Breakdown characteristics in pulsed-driven dielectric barrier discharges: influence of the pre-breakdown phase due to volume memory effects *Journal of Physics D-Applied Physics* **47** 465206

[10] Bourdon A, Bonaventura Z and Celestin S 2010 Influence of the pre-ionization background and simulation of the optical emission of a streamer discharge in preheated air at atmospheric pressure between two point electrodes *Plasma Sources Science & Technology* **19** 034012

[11] Shao T, Sun G S, Yan P, Wang J, Yuan W Q, Sun Y H and Zhang S C 2006 An experimental investigation of repetitive nanosecond-pulse breakdown in air *Journal of Physics D-Applied Physics* **39** 2192-2197

[12] Acker F E and Penney G W 1968 Influence of previous positive streamers on streamer propagation and breakdown in a positive point - to - plane gap *Journal of Applied Physics* **39** 2363-2369

[13] Xu D A, Lacoste D A, Rusterholtz D L, Elias P Q, Stancu G D and Laux C O 2011 Experimental study of the hydrodynamic expansion following a nanosecond repetitively pulsed discharge in air *Applied Physics Letters* **99** 121502

[14] Davydov S G, Dolgov A N, Kozlov A A, Revazov V O and Yakubov R K 2024 Fast Shadow Visualization of a Pulsed Discharge in a Short Gas Gap *Technical Physics* **69** 169-180

[15] Lambert J, Coulombe S, Bourque G and Bergthorson J 2023 Hydrodynamic effect of nanosecond repetitively pulsed discharges produced throughout a laminar stagnation flame *Applications in Energy and Combustion Science* **14** 100130

[16] Naidis G V 2008 Simulation of spark discharges in high-pressure air sustained by repetitive high-voltage nanosecond pulses *Journal of Physics D-Applied Physics* **41** 234017

[17] Tholin F and Bourdon A 2013 Simulation of the stable 'quasi-periodic' glow regime of a nanosecond repetitively pulsed discharge in air at atmospheric pressure *Plasma Sources Science & Technology* **22** 045014

[18] Tholin F and Bourdon A 2013 Simulation of the hydrodynamic expansion following a nanosecond pulsed spark discharge in air at atmospheric pressure *Journal of Physics D-Applied Physics* **46** 365205

[19] Yuan X C, Li H W, Abbas M F, Li X R, Wang Z, Zhang G J and Sun A B 2020 A 3D numerical study of positive streamers interacting with localized plasma regions *Journal of Physics D-Applied Physics* **53** 425204

[20] Zhao Z, Li C J, Guo Y L, Zheng X L, Sun A B and Li J T 2023 Streamer dynamics and periodical discharge regime transitions under repetitive nanosecond pulses with airflow *Plasma Sources Science & Technology* **32** 015002

[21] Nijdam S, Takahashi E, Markosyan A H and Ebert U 2014 Investigation of positive streamers by double-pulse experiments, effects of repetition rate and gas mixture *Plasma Sources*

Science & Technology **23** 025008

[22] Li Y, van Veldhuizen E M, Zhang G J, Ebert U and Nijdam S 2018 Positive double-pulse streamers: how pulse-to-pulse delay influences initiation and propagation of subsequent discharges *Plasma Sources Science & Technology* **27** 125003

[23] Kazemi M R, Sugai T, Tokuchi A and Jiang W H 2017 Study of Pulsed Atmospheric Discharge Using Solid-State LTD *Ieee Transactions on Plasma Science* **45** 2323-2327

[24] Zhang X, Guo Y L, Mirpour S, Li Y R, Sun A B and Nijdam S 2021 Effects of a negative corona discharge on subsequent positive streamers *Journal of Physics D-Applied Physics* **54** 485202

[25] Chen X C, Zhu Y F and Wu Y 2020 Modeling of streamer-to-spark transitions in the first pulse and the post discharge stage *Plasma Sources Science & Technology* **29** 095006

[26] Malla H, Martinez A, Ebert U and Teunissen J 2023 Double-pulse streamer simulations for varying interpulse times in air *Plasma Sources Science & Technology* **32** 095006

[27] Zhu Y F, Shcherbanev S, Baron B and Starikovskaia S 2017 Nanosecond surface dielectric barrier discharge in atmospheric pressure air: I. measurements and 2D modeling of morphology, propagation and hydrodynamic perturbations *Plasma Sources Science & Technology* **26** 125004

[28] Grubert G K, Becker M M and Loffhagen D 2009 Why the local-mean-energy approximation should be used in hydrodynamic plasma descriptions instead of the local-field approximation *Physical Review E* **80** 036405

[29] Zhu Y F, Chen X C, Wu Y, Hao J B, Ma X G, Lu P F and Tardiveau P 2021 Simulation of ionization-wave discharges: a direct comparison between the fluid model and E-FISH measurements *Plasma Sources Science & Technology* **30** 075025

[30] Guo Y L, Li Y R, Zhu Y F and Sun A B 2023 A numerical and experimental study on positive diffusive ionization waves in different N₂/O₂ mixtures: the role of photoionization *Plasma Sources Science & Technology* **32** 025003

[31] Brisset A, Gazeli K, Magne L, Pasquiers S, Jeanney P, Marode E and Tardiveau P 2019 Modification of the electric field distribution in a diffuse streamer-induced discharge under extreme overvoltage *Plasma Sources Science & Technology* **28** 055016

[32] Chng T L, Pai D Z, Guaitella O, Starikovskaia S M and Bourdon A 2022 Effect of the electric field profile on the accuracy of E-FISH measurements in ionization waves *Plasma Sources Science & Technology* **31** 015010

[33] Guo B H and Teunissen J 2023 A computational study on the energy efficiency of species production by single-pulse streamers in air *Plasma Sources Science & Technology* **32** 025001

[34] Tardiveau P, Magne L, Marode E, Ouaras K, Jeanney P and Bournonville B 2016 Sub-nanosecond time resolved light emission study for diffuse discharges in air under steep high voltage pulses *Plasma Sources Science & Technology* **25** 054005

[35] Briels T M P, van Veldhuizen E M and Ebert U 2008 Positive streamers in air and nitrogen of varying density: experiments on similarity laws *Journal of Physics D-Applied Physics* **41** 234008

[36] Pancheshnyi S 2015 Photoionization produced by low-current discharges in O₂, air, N₂ and CO₂ *Plasma Sources Science & Technology* **24** 015023

[37] Briels T M P, van Veldhuizen E M and Ebert U 2008 Time resolved measurements of streamer inception in air *Ieee Transactions on Plasma Science* **36** 908-909

[38] Nijdam S, Miermans K, van Veldhuizen E M and Ebert U 2011 A Peculiar Streamer Morphology Created by a Complex Voltage Pulse *Ieee Transactions on Plasma Science* **39** 2216-2217

[39] Nijdam S, Teunissen J and Ebert U 2020 The physics of streamer discharge phenomena *Plasma Sources Science & Technology* **29** 103001

[40] Chen S, Heijmans L C J, Zeng R, Nijdam S and Ebert U 2015 Nanosecond repetitively pulsed discharges in N₂-O₂ mixtures: inception cloud and streamer emergence *Journal of Physics D-Applied Physics* **48** 175201

[41] Ren C H, Huang B D, Zhang C, Qi B, Chen W J and Shao T 2023 The critical effect of electron acceleration under enhanced electric field near cathode on the formation of runaway electrons and diffuse discharge in atmosphere *Plasma Sources Science & Technology* **32** 085013

[42] Ebert U, Brau F, Derks G, Hundsdorfer W, Kao C Y, Li C, Luque A, Meulenbroek B, Nijdam S, Ratushnaya V, Schäfer L and Tanveer S 2011 Multiple scales in streamer discharges, with an emphasis on moving boundary approximations *Nonlinearity* **24** C1-C26

[43] Arrayás M, Ebert U and Hundsdorfer W 2002 Spontaneous branching of anode-directed streamers between planar electrodes -: art. no. 174502 *Physical Review Letters* **88** 174502

[44] Meulenbroek B, Rocco A and Ebert U 2004 Streamer branching rationalized by conformal mapping techniques *Physical Review E* **69** 067402

[45] Babaeva N Y and Naidis G V 1996 Two-dimensional modelling of positive streamer dynamics in non-uniform electric fields in air *Journal of Physics D-Applied Physics* **29** 2423-2431

[46] *Phelps database (N2, O2) www.lxcat.net (retrieved 19 January 2021)*

[47] Kossyi I A, Kostinsky A Y, Matveyev A A and Silakov V P 1992 Kinetic scheme of the non-equilibrium discharge in nitrogen-oxygen mixtures *Plasma Sources Science & Technology* **1** 207-220

[48] Hayashi M "Personal communication to the JILA atomic collisions data center" 1987.

[49] Babaeva N Y and Naidis G 2018 Modeling of streamer interaction with localized plasma regions *Plasma Sources Science and Technology* **27** 075018

[50] Ono R and Ishikawa Y 2018 The effect of temperature on pulsed positive streamer discharges in air over the range 292 K-1438 K *Journal of Physics D-Applied Physics* **51** 185204

[51] Laux C O, Kruger C H and Zare R N 2001 Diagnostics of atmospheric pressure air plasmas *APP Spring Meeting `Diagnostics of Non-Equilibrium High Pressure Plasmas' Book of Papers* 101-113

[52] Brisset A, Tardiveau P, Gazeli K, Bournonville B, Jeanney P, Ouaras K, Magne L and Pasquiers S 2021 Experimental study of the effect of water vapor on dynamics of a high electric field non-equilibrium diffuse discharge in air *Journal of Physics D-Applied Physics* **54** 215204

[53] Brisset A, Guichard F, Cessou A and Tardiveau P 2021 Energy relaxation and heating in the afterglow of high electric field ns-discharges in ambient air using spontaneous Raman scattering *Plasma Sources Science & Technology* **30** 035013

[54] Montello A, Yin Z, Burnette D, Adamovich I V and Lempert W R 2013 Picosecond CARS measurements of nitrogen vibrational loading and rotational/translational temperature in non-equilibrium discharges *Journal of Physics D-Applied Physics* **46** 464002

[55] Montello A D *Studies of Nitrogen Vibrational Distribution Function and Rotational-*

Translational Temperature in Nonequilibrium Plasmas by Picosecond Coherent Anti-Stokes Raman Scattering Spectroscopy, 2012

[56] Heijmans L C J, Clevis T T J, Nijdam S, van Veldhuizen E M and Ebert U 2015 Streamer knotwilg branching: sudden transition in morphology of positive streamers in high-purity nitrogen *Journal of Physics D-Applied Physics* **48** 355202

[57] Kosarev I N, Starikovskiy A Y and Aleksandrov N L 2019 Development of high-voltage nanosecond discharge in strongly non-uniform gas *Plasma Sources Science & Technology* **28** 015005

[58] Ono R and Oda T 2004 Visualization of streamer channels and shock waves generated by positive pulsed corona discharge using laser schlieren method *Japanese Journal of Applied Physics Part 1-Regular Papers Brief Communications & Review Papers* **43** 321-327

[59] Guo B H, Ebert U and Teunissen J 2023 3D modeling of positive streamers in air with inhomogeneous density *Plasma Sources Science & Technology* **32** 095015

[60] Komuro A, Tsukada H and Ando A 2019 Slow Gas Heating Process in an Atmospheric-Pressure Streamer Discharge Visualized by High-Speed Schlieren Method *Ieee Transactions on Plasma Science* **47** 1164-1171

[61] Phelps A V and Pitchford L C 1985 ANISOTROPIC SCATTERING OF ELECTRONS BY N-2 AND ITS EFFECT ON ELECTRON-TRANSPORT *Physical Review A* **31** 2932-2949

[62] Lawton S A and Phelps A V 1978 Excitation of the b 1Σ+g state of O2 by low energy electrons *The Journal of Chemical Physics* **69** 1055-1068

[63] Pancheshnyi S 2013 Effective ionization rate in nitrogen-oxygen mixtures *Journal of Physics D-Applied Physics* **46** 155201

[64] Popov N A 2011 Fast gas heating in a nitrogen-oxygen discharge plasma: I. Kinetic mechanism *Journal of Physics D-Applied Physics* **44** 285201

[65] Pancheshnyi S, Nudnova M and Starikovskii A 2005 Development of a cathode-directed streamer discharge in air at different pressures: Experiment and comparison with direct numerical simulation *Physical Review E* **71** 016407